Multiresolution Homogenization of Field and Network Formulations for Multiscale Laminate Dielectric Slabs—Part I: Field Theory

Vitaliy Lomakin, Ben Z. Steinberg, *Senior Member, IEEE*, Ehud Heyman, *Fellow, IEEE*, and Leopold B. Felsen, *Life Fellow, IEEE*

***Abstract*—Conventional theories addressing the wave-dynamic behavior of plane-stratified multilayer environments usually involve wavenumber spectral and asymptotic techniques, which apply to layer thickness of the same "macroscale" order as the wavelengths in the spectrum of the excitation. However, in applications of multilayer bonded laminates (for example, in biological and other "exotic" materials") wherein the layer structure contains extremely fine "microscale" constituents as well as the conventional macroscales, the desired "observables" involve the macroscale response, which accounts self-consistently for the macroscale loading by the microscales. A novel *multiresolution homogenization* (MRH) has been presented previously to provide the self-consistent rigorous analytic micro-macro scale framework for calibrated parameterization of the wave dynamics in terms of a microscale-loaded macroscale medium with corresponding "effective" field observables. The outcome has been an algorithm that allows the conversion of the conventional macroscale propagation models to their "effective" micro-macroscale versions by *direct substitution* of the MRH-based effective fields, media, etc., in place of the corresponding conventional quantities, with error bounds that quantify the quality of the substitution. This theory may accommodate broad ranges, discrete and continuous, of wavenumber spectra and thus can be applied in conjunction with the spectral techniques noted above. In this paper, relevant "pragmatic" results of the MRH-based field theory are extracted from the previous formal treatment and are extended to accommodate alternative physics-matched MRH field representations. The reflection, transmission, and waveguiding properties, in free space, of a dipole-excited laminate slab whose scales span a wide continuum from micro to macro are examined in detail, with emphasis on alternative MRH field representations (ray, guided mode, etc.) that are best matched to the wave physics for specified ranges of operating frequencies, source-observer locations, etc. Extensive numerical experiments have been performed to calibrate, via quantified error bounds, the quality and range of validity of the conventional-to-MRH conversion for these alternative field representations. This lays the foundation for an MRH-based *effective network* theory for multiscale laminate conglomerates comprising a sequence of *micro-macroscale laminate* constituents, to be presented in Part II of this paper.**

***Index Terms*—Effective properties, layered media, medium complexity, multiresolution homogenization, wavelets.**

Manuscript received June 11, 2002. This work was supported in part by the US-Israel Binational Science Foundation, Jerusalem, Israel, under Grant 9900448 and in part by the Israel Ministry of Science. The work of L. B. Felsen was supported in part by ODDR&E under MURI Grants ARO DAAG55-97-1-0013 and AFOSRF49620-1-0028, in part by the Engineering Research Centers Program of the National Science Foundation under Award EEC-9986821, and in part by Polytechnic University, Brooklyn, NY.

V. Lomakin was with the Department of Interdisciplinary Studies, Faculty of Engineering, Tel Aviv University, 69978 Tel Aviv, Israel. He is now with the Center for Computational Electromagnetics, University of Illinois at Urbana-Champaign, Urbana, IL 61801-2991 USA (e-mail: vitaliy@emlab.uiuc.edu).

B. Z. Steinberg and E. Heyman are with the School of Electrical Engineering, Tel Aviv University, 69978 Tel Aviv, Israel (e-mail: steinber@eng.tau.ac.il; heyman@eng.tau.ac.il).

L. B. Felsen is with the Department of Aerospace and Mechanical Engineering and Department of Electrical and Computer Engineering, Boston University, Boston, MA 02215 USA and with the Polytechnic University, Brooklyn, NY 11201 USA.

Digital Object Identifier 10.1109/TAP.2003.816356

I. Introduction

A. Background Perspectives

DISCRETE/continuous plane stratified media have long served as models for the study of wave propagation in diverse natural and man-made complex environments. The solution strategy for this "conventional" class of problems has been the use of alternative problem-matched discrete/continuous transforms from the three-dimensional (3-D) actual (physical) domain to the appropriate 1-D or 2-D wavenumber spectral domains; this procedure decomposes the original source-excited wavefield into superpositions of simpler wave types in the corresponding 2-D or 1-D spectral subdomains, respectively. The wave species in the spectral domain can broadly be grouped into complementary *progressing* (ray-type) and *oscillatory* (mode-type) categories, which are characterized by their distinct wavenumber spectral footprints. A self-consistent hybrid ray-mode (progressing-oscillatory) formulation has been constructed to exploit the most favorable characteristics of each [1]–[5]. For further details on related spectral techniques, see also [6]–[13].

The description above refers essentially to the *macro* (or large-scale) properties of the multilayer ambient medium, where the thickness of the layers is of the same macro order over the prevailing frequency spectrum. However, in many situations, the medium is characterized also by a rich variety of *micro* structures whose effect on the macro field equations and the ensuing field structure needs to be attended to. Such multiscale laminates can serve as models for certain fabricated composite materials with micro bonding regions between macro layers, dense electronic circuits, geophysical environments, biological media, etc. In most cases, one is interested only in the macro field observables (which, however, incorporate the microscale effects), either because they dominate the field (e.g., in the far zone) or because of the macro measurement setup (e.g., the space-time integration window of the detector). This paper presents a *self-consistent* scale-based *multiresolution*

homogenization (MRH) procedure for finely multiscale *laminates* that bridges the gap between the macro- and micro-scale field phenomena, and shows how one may adapt the arsenal of parameterization techniques for conventional macro-type wave problems discussed above to describe wave interactions with complex multiscale structures.

Traditional homogenization schemes have been developed for periodic micro structures (see, e.g., [14] and [15]) and deal essentially with the bulk properties of the homogenized media, assuming space-invariant effective properties. A multiresolution approach for *numerical* homogenization, and for calculating the large-scale response, has been introduced in [16]–[18], using a sophisticated "decimation" algorithm, but the analysis has remained on the level of the corresponding matrix equation without recourse to an *effective formulation* involving effective medium and boundary conditions.

In the MRH theory here, the medium and the resulting field equations are decomposed into binary-based scales via the theory of *multiresolution decomposition* (MRD) [19], [20] and are then solved self-consistently in the desired resolution scale. The theory makes a distinction between the *field homogenization scale* (F-HS) 2^{-j} and the *medium homogenization scale* (M-HS) $2^{-\nu}$, which is typically smaller (i.e., $\nu \geq j$). The F-HS defines the resolution space $\mathbb{V}_j$, which contains the relevant "physical observables" chosen by the wave modeler, and whose scale is larger than the F-HS. The effect of all neglected micro scales is embedded within an effective material operator (EMO), which describes the couplings between the micro-scale components in the medium heterogeneity and the field response in the observable space $\mathbb{V}_j$. The EMO, through its bound, formalizes and quantifies the error in $\mathbb{V}_j$ between the "actual" (or true) field observables and those predicted by the "effective" theory for a given HS. Unlike traditional homogenization procedures [14], [15], the novel two-scales MRH can deal with nonperiodic structures and is *not* a perturbation theory that requires weak micro heterogeneities or a scale-gap between the macro and micro heterogeneities. This property is due to the fact that the ratio (M-HS/F-HS) between the scale of the medium homogenization and the relatively larger scale of the observables is an inherent small parameter that governs the bound on the error in the observables space $\mathbb{V}_j$. This allows the MRH to accommodate media with continuous distributions of scales, thereby facilitating the choice of homogenization scale that best models the physics of the problem, as well as control of the actual-effective formulation error. For example, the continuous distribution property is relevant for ultra-wide-band (UWB) excitation scenarios, where it is desirable to change the HS in accord with the wavelength, or for localized sources in 3-D configurations where the HS should accommodate the spectral wavenumbers. The theory is accompanied by comprehensive error analysis, with explicit expressions for the error bounds in terms of dimensionless estimators that clearly identify and quantify all sources of error in the homogenization, and it may be applied in general to uniaxial media wherein both ε and μ can be multiscale "messy" heterogeneous functions.

The principal concepts and mathematical foundations pertaining to the MRH were introduced originally in [21]–[27]. The theory has been generalized and refined in [28]–[31] by introducing the two-scales formulation; a two-step Green's function procedure for dealing with several heterogeneity functions; and a more accessible formulation for the error bounds in terms of the norm of the micro heterogeneity (rather than its degree of regularity as in [25]–[27]). Furthermore, the theory now contains the complete spectral expansion of the wave operator expressed in the observables space $\mathbb{V}_j$. Consequently the MRH can now deal with three-dimensional source-excited electromagnetic (EM) problems (e.g., obtain EM Green's functions) in bounded or nonbounded plane-layered multiscale laminate configurations making use of the extensive toolbox of spatial-spectral parameterization techniques described in the first paragraph and its cited references (see, e.g., [27], [32], and [33]).

B. This Investigation

Building upon the previous investigations in Section I-A, we are now planning a systematic sequence of studies focused on radiation from, guiding within, and junctions between different multilayer micro/macroscale composite slab configurations characterized by their "effective" equivalents, and on "effective" *field-network* (transmission line) models for such conglomerates. The goal is a validated "pragmatic" approximate formulation that permits the "effective" field-network description of a multiscale laminate conglomerate to be obtained by direct substitution of the homogenized "effective" fields, media, etc., into available corresponding formulations for their conventional macro counterparts. Our adopted format toward learning the rules is a two-part sequence concerned with the MRH treatment of network-matched Green's functions (GFs) for typical multiconstituent multiscale plane-layered laminate slab configurations. This paper deals with the *field theory* for a typical constituent within this framework. The corresponding MRH-parameterized *network relations* will appear in Part II of this paper [34].

Two broad objectives guide this presentation.

1) To extract from the comprehensive and heavily mathematical treatment in [28] and [29] those "pragmatic" results that are required to perform the above-mentioned planned extensions.
2)
   a) To extend the scope of the "basic" MRH Green's functions in [28] and [29] so as to match the GFs (via appropriate boundary conditions) to *alternative* useful network representations to be explored in Part II.
   b) To produce a comprehensive *synthetic data base* for a typical multiscale laminate example by numerical experimentation over problem parameter ranges selected so as to demonstrate the parametric sensitivity of the perceived wave physics and of the overall performance of our model, thereby establishing understanding of, and confidence in, our calibrated analytic error quantifications for the actual/effective equivalence.

Item 2a) and the laminate model in 2b) are new and have not been explored in [28] and [29].

In this paper, Section II contains the description of the actual problem environment and the definition of the MRH-smoothed "effective" field observables. Section III is concerned with the details of the effective 3-D vector field problem:

1) the 2-D vector mode decomposition of the field in the (x, y) cross-section parallel to the stratification and the resulting spectral transmission-line (TL) formulations along the z-axis for the actual and effective modal amplitudes in the effective medium (Section III-A);
2) the quality assessment of the desired equivalence between the actual and effective field amplitudes by quantitative error bounds (Section III-B);
3) derivation of the MRH via formal MRD of the TL equations into macro (smooth) and micro (detail) components, with absorption of the micro scales within the macro-scale format via the EMO (Section III-C).

Section IV is concerned with the construction of the effective spectra of the TL equations along the z-axis, utilizing the "characteristic" GF procedure in [6, ch. 3], and with the quality assessment (via error bounds) of the spectral equivalence between the actual and effective spectra. Included are the construction of the complete (discrete and continuous) spectrum of the multiscale wave equation and the definition of the relevant (or effective) and nonrelevant (detailed) parts of the spectrum within a prescribed formulation accuracy. This section also contains the new extension to network-matched alternative GF representations. The results are utilized in Section V for the spectral synthesis and quality assessment of the 3-D effective GFs for the total field. In Section VI, the various spectral domain and total field effective formulations and their analytic quality assessments, developed in Sections II–V, are validated further by new extensive "actual" versus "effective" calibrated numerical comparisons for our chosen laminate model. Concluding remarks are presented in Section VII.

II. Statement of the Problem

A. Physical Configuration

We consider source-excited electromagnetic fields in complex laminates characterized by multiscale (macro/micro) heterogeneities along the stratification axis z. The propagation domain may have any bounded or unbounded cross-section perpendicular to the z-axis (Fig. 1). Two special cases are a *transversely unbounded* complex laminated slab and a *transversely bounded* waveguide filled with a complex laminate. The laminate is located in $0 < z < d$ and generally has penetrable boundaries that grant access to the surrounding homogeneous media in $z < 0$ and $z > d$. The normalized laminate constitutive parameters may be diagonal tensors whose components $(\varepsilon_z, \varepsilon_t)$ and (μ_z, μ_t) (where the subscripts denote the z and transverse to z components) are *multiscale* functions of z that comprise both macro and micro scales. The field is excited by a current distribution $\mathbf{J}(\mathbf{r})$ located either inside or outside the laminate, and a monochromatic time dependence $e^{-i\omega t}$ is assumed and suppressed; the frequency or time dependencies will be displayed explicitly only under conditions of wide-band excitation [30]. Boldface symbols denote vector quantities.

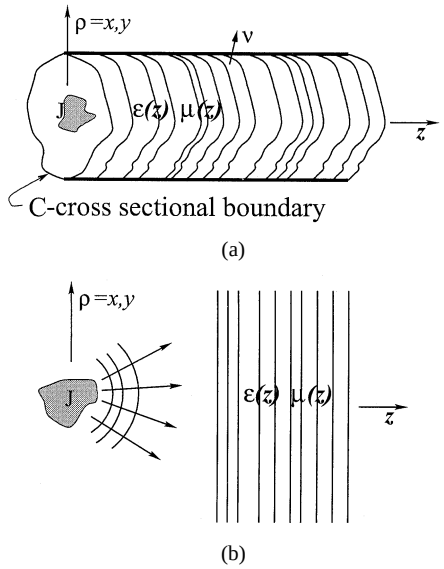

Fig. 1. Problem formulation: (a) waveguide filled with a complex laminate and (b) a complex laminate slab.

B. Smoothed Effective Field Observables: MRH

To implement our stated objective of generalizing conventional field-network theory so as to include "effective" field and medium characterization of multiscale laminate configurations, we require previously obtained results from MRH, which are summarized below.

1) Macro- and Micro-Scale Parameterization: An effective formulation for the *macro-scale field* smooths out the micro-scale heterogeneities while retaining their effect on the macro-scale observables. Although the multiscale structure of the medium induces multiscale components in the 3-D electromagnetic field, the relevant field *observables* are described on a scale that is typically determined by the *wave physics* (e.g., the wavelength, near/far fields) or by the measurement arrangement (e.g., the spatiotemporal resolution of the detector, the dynamic range and the polarization, etc.). Accounting for these aspects permits simplification of the field calculations through retention of only the large-scale components of the response, which thus define the *field homogenization scale*. We shall choose the F-HS according to the wave physics. The most basic scale is characterized by the *local effective wavenumber* in the material; i.e., F-HS$= (k_0\sqrt{\varepsilon_{\max}\mu_{\max}})^{-1}$, with $k_0 = \omega/c$ being the free-space wavelength at the frequency ω [see (8) and (9) for a precise definition]. However, in waveguiding configurations, the waveguide width motivates consideration of a *larger* F-HS. Thus, for frequencies high enough to support *propagating* modes transverse to z in the slab configuration of Fig. 1(b), the relevant scale for such a mode is its spectral wavenumber $d/2\pi l$ where $l = 1, 2, \ldots$ is the mode index and d is the slab width (for further details, see Section V). The resulting (F-HS$\sim (d/2\pi \subset)$ even for the lowest order propagating modes may now be much larger than $(k_0\sqrt{\varepsilon_{\max}\mu_{\max}})^{-1}$. On the other hand, if one is interested in the field in the source region, the F-HS might be much smaller, and would be determined essentially by the detector size.

Having chosen a relevant field homogenization scale, we invoke the theory of multiscale resolution decomposition [19]

(which is briefly summarized in the Appendix) to parameterize the F-HS macro and micro components in terms of the binary scale basis

$$\text{F–HS} = \bar{d}2^{-j}, \quad j = \text{integer} \tag{1}$$

where $\bar{d}$ is an arbitrary reference scale. A given field function $f(z)$ is thereby decomposed into its "smooth" (macro-scale) and "detailed" (micro-scale) orthogonal components f^s and f^d, respectively, via the projection operators $\mathcal{P}_j$ and $\mathcal{D}_j$ defined in (A5). $\mathcal{P}_j$ projects f onto the linear (field amplitude) spaces $\mathbb{V}_j \subset \mathbb{L}_2$ containing all scales $\geq \bar{d}2^{-j}$, while $\mathcal{D}_j$ projects f onto the orthogonal complementary space $\bigcup_{m=j}^{\infty} \mathbb{W}_m$ $(m = \text{integer})$ that contains all smaller scales; the wavelet space $\mathbb{W}_m$ consists only of the scale $\bar{d}2^{-m-1}$. The sets of scaling and wavelets functions $\{\phi_{jn}\}_{n\in\mathbb{Z}}$ and $\{\psi_{mn}\}_{n\in\mathbb{Z}}$, with $\mathbb{Z}$ being the set of all integers, constitutes a basis of the *homogenization space* (or *observables space*) $\mathbb{V}_j$ and of $\mathbb{W}_m$, respectively.

2) Smoothed Approximation of the Actual Field: Having determined the F-HS, we are interested only in the smoothed field observables, and the corresponding "effective" medium that describes these observables. This is accomplished by projecting the "actual" field ($\mathbf{E}$, $\mathbf{H}$) onto $\mathbb{V}_j$, and is formalized by the condition

$$\mathcal{P}_j(\mathbf{E}^{\text{ef}}, \mathbf{H}^{\text{ef}}) = \mathcal{P}_j(\mathbf{E}, \mathbf{H}). \tag{2}$$

The challenge to the modeler is to choose the effective medium consistent with this requirement as simply as possible so as to allow efficient numerical evaluation of the field and a cogent interpretation of the "effective" wave physics. The quality of this formulation to within a prescribed error needs to be established in the homogenization space of physical observables.

III. Effective Field Problem

A. Actual Field: Wavenumber Spectral Representation and Source-Excited Transmission Line Formulation

The configurations in Fig. 1 can be analyzed via modal decomposition and transmission-line theory [6, ch. 2]. The actual vector field is expressed as a spectral superposition (discrete and/or continuous) of both E (TM)- and H (TE)-type modes, tagged by the superscript $\alpha = e$ or h, respectively. Its transverse-to-z components (t) are given by the spectral summations

$$\mathbf{E}_t(\mathbf{r}) = \sum_{\alpha=e,h} \sum_{\boldsymbol{\xi}} V^{\alpha}(z,\xi)\mathbf{e}^{\alpha}(\boldsymbol{\rho},\boldsymbol{\xi}) \tag{3a}$$

$$\mathbf{H}_t(\mathbf{r}) = \eta^{-1} \sum_{\alpha=e,h} \sum_{\boldsymbol{\xi}} I^{\alpha}(z,\xi)\mathbf{h}^{\alpha}(\boldsymbol{\rho},\boldsymbol{\xi}) \tag{3b}$$

where $\eta = \sqrt{(\mu_0/\varepsilon_0)}$. Here $\mathbf{r} = (x,y,z) = (\boldsymbol{\rho}, z)$ denotes the 3-D coordinate, with $\boldsymbol{\rho}$ denoting the coordinates transverse to z; $\boldsymbol{\xi} = (\xi_x, \xi_y)$ identifies the vector transverse wavenumber spectral coordinates with $\xi \equiv |\boldsymbol{\xi}\cdot\boldsymbol{\xi}|^{1/2}$; and $\mathbf{e}^{\alpha}$ and $\mathbf{h}^{\alpha} = \hat{\mathbf{z}} \times \mathbf{e}^{\alpha}$ are the vector mode functions corresponding to the spectral parameter $\boldsymbol{\xi}$ and the α mode-type, and they are normalized such that $\int\int d^2\boldsymbol{\rho}\mathbf{e}^{\alpha *}(\boldsymbol{\rho},\boldsymbol{\xi}) \cdot \mathbf{e}^{\alpha}(\boldsymbol{\rho},\boldsymbol{\xi}') = \delta_{\boldsymbol{\xi},\boldsymbol{\xi}'}$ (Kronecker's delta), where the integration is performed over the cross-section and the asterisk $*$ denotes the complex conjugate. It is convenient to use $\boldsymbol{\xi}$ as a dimensionless frequency-normalized spectral parameter (i.e., the transverse wavenumber is given by $\mathbf{k}_t = k_0\boldsymbol{\xi}$).

The spectral voltage and current *amplitudes* (V, I) of (3) excited by the spectral *sources* (v^{α}, i^{α}) corresponding to $\mathbf{J}(\mathbf{r})$ are found via the *spectral transmission-line* equations in the heterogeneous medium (here assumed to be uniaxially anisotropic)

$$\frac{d}{dz}V^{\alpha} = ik_0 pI^{\alpha} - v^{\alpha} \tag{4a}$$

$$\frac{d}{dz}I^{\alpha} = ik_0 qV^{\alpha} - i^{\alpha} \tag{4b}$$

with (V^{α}, I^{α}) continuous across interface discontinuities. In (4), the (multiscale) heterogeneity functions $p = p(z,\boldsymbol{\xi})$ and $q = q(z,\boldsymbol{\xi})$ are given by [28]

$$\text{E modes}: \quad p(z,\boldsymbol{\xi}) = \mu_t - \varepsilon_z^{-1}\xi^2, \quad q = \varepsilon_t \tag{5a}$$

$$\text{H modes}: \quad q(z,\boldsymbol{\xi}) = \varepsilon_t - \mu_z^{-1}\xi^2, \quad p = \mu_t \tag{5b}$$

where $\varepsilon_{t,z}$ and $\mu_{t,z}$ are the (transverse, longitudinal) medium permittivity and permeability, respectively. Moreover, $k_0\sqrt{pq}$ and $\sqrt{p/q}$ represent, respectively, the local spectral wavenumber (propagation coefficient) and characteristic impedance along z. Note that the formulation in (4) is normalized differently from what is conventional [6]. In view of the η^{-1} factor in (3b), both V and I in (4) are measured in volts, while p and q are dimensionless.

B. Effective Field: Effective Spectral Transmission Line and Effective Medium Formulations

1) Construction of the Effective Formulations: Referring to the spectral TL equations (4), we are interested in finding a simplified effective medium with smoother parameters (p^{ef}, q^{ef}). The modal field amplitudes (V^{ef}, I^{ef}) in this medium satisfy effective TL equations, which are given by (4) but with (p, q) replaced by (p^{ef}, q^{ef}). Referring to (2), this implies equality of the projections $\mathcal{P}_j(V^{\text{ef}}, I^{\text{ef}}) = \mathcal{P}_j(V, I)$ of the actual and effective modal amplitudes to within tolerable prescribed error bounds. It can be shown that the equality is satisfied up to a specified error if one neglects all scales in the heterogeneity functions of (5) that are smaller than the *medium homogenization scale* (M-HS)

$$\text{M–HS} = \bar{d}2^{-\nu}, \quad \nu = \text{integer} \tag{6}$$

i.e., the M-HS defines the *smallest* scale in the effective (homogenized) medium. The M-HS is typically finer than the F-HS but should be chosen as large as is tolerably possible in order to simplify (by reducing the number of basis functions) the effective medium description. The effective and detail (neglected) parts of the medium are given by the respective projections

$$(p^{\text{ef}}, q^{\text{ef}}) = \mathcal{P}_{\text{M}}(p,q), \quad (p^d, q^d) = \mathcal{D}_{\nu}(p,q), \quad M \geq \nu \tag{7}$$

where $M = \nu$, in general, except for cases where there is a scale-gap in the medium; in that case the scale $\bar{d}2^{-M}$ of the effective medium can be larger than $\bar{d}2^{-\nu}$. To clarify these considerations, we refer to Fig. 2, which describes two typical media. Medium 1 possesses a continuum of scales from macro to micro, whence $M = \nu$ and the M-HS is chosen so as to render the error bound for the effective formulation "sufficiently small."

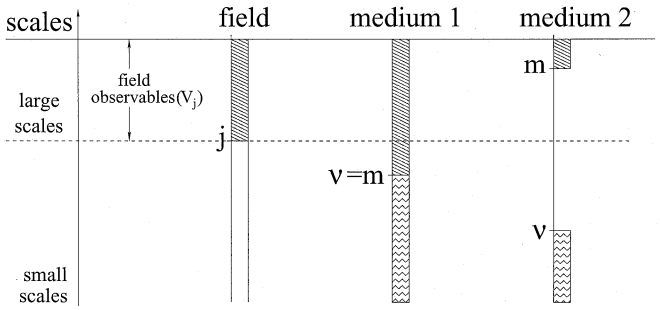

Fig. 2. MRA scales: the field homogenization scale (F-HS) separates the field into scales larger and smaller than 2^{-j} and is typically determined by the operating wavelength. The medium homogenization scale (M-HS) removes all heterogeneity scales smaller than $2^{-\nu}$, where $\nu < j$. The scale ratio $N_\nu \leq (\text{M–HS}/\text{F–HS}) = 2^{-(\nu-j)}$ controls the error (see (11)). If the medium has a scale-gap as sketched in Medium 2, then the M-HS can be taken to be m, which is greater than $j < \nu$ (yielding a simpler medium representation). Here, too, the error is controlled by ν, which represents the largest scale of the detailed heterogeneity that is neglected in the homogenization.

Medium 2, on the other hand, has a gap between the macro and micro scales around the F-HS, whence ν is still determined by the above error bound but the effective medium is described more efficiently by the smallest scale above the gap, denoted in Fig. 2 and in (7) by the index M.

Substituting (7) into (5), one finds that the homogenized *effective constitutive parameters* are given by

$$\begin{aligned} \varepsilon_t^{\text{ef}} &= \mathcal{P}_M \varepsilon_t, \\ \mu_t^{\text{ef}} &= \mathcal{P}_M \mu_t \end{aligned} \tag{8a}$$

$$\begin{aligned} \varepsilon_z^{\text{ef}} &= \left[\mathcal{P}_M \left(\varepsilon_z^{-1}\right)\right]^{-1} \\ \mu_z^{\text{ef}} &= \left[\mathcal{P}_M \left(\mu_z^{-1}\right)\right]^{-1} \end{aligned} \tag{8b}$$

which implies an *effective anisotropy* (e.g., $\varepsilon_t^{\text{ef}} \neq \varepsilon_z^{\text{ef}}$ even if $\varepsilon_t = \varepsilon_z$). See samples in Figs. 3 and Fig. 4, which are further discussed in Section VI-A.

2) Quality Assessment of the Effective Formulations: Error Bounds: The quality of the effective spectral formulations has been tested in observables space $\mathbb{V}_j$ where field variations on scales smaller than the F-HS are not resolved. These variations are incorporated in the effective spectral wavenumber in the z direction, $\kappa^{\text{ef}}(z) = k_0\sqrt{p^{\text{ef}}q^{\text{ef}}}$ [see (4) with (5)]. We therefore introduce the dimensionless bound

$$K(\xi) = \max_z \sqrt{|p^{\text{ef}}(z)q^{\text{ef}}(z)|} \tag{9}$$

and note that in the evanescent regime (where either p^{ef} or q^{ef} becomes negative), $K(\xi)$ tends to infinity like $\sim O(\xi)$ for large ξ. Thus the projection of (V, I) onto $\mathcal{P}_j$ retains only the contributions from the *relevant* (i.e., "visible") spectral range

$$\text{F–HS} \leq [k_0 K(\xi)]^{-1} \tag{10}$$

with diminishing contribution from all other spectral regimes with larger $K(\xi)$. For a given F-HS, (10) therefore defines the *relevant* spectral range. If the F-HS is chosen as $(k_0\sqrt{\varepsilon_{\max}^{\text{ef}}\mu_{\max}^{\text{ef}}})^{-1}$, characteristic of the bulk medium properties, then the relevant range, in terms of the homogenization, coincides with the visible range where $|\xi| \leq \sqrt{\varepsilon_{\max}^{\text{ef}}\mu_{\max}^{\text{ef}}}$. In this case $K(\xi)$ is bounded by its maximal value that occurs at $\xi = 0$, i.e., $K(\xi) \leq \sqrt{\varepsilon_{\max}\mu_{\max}}$. If, on the other hand, one is interested only in an effective formulation for the dominant (propagating) *modes* in a *waveguiding configuration* [see discussion preceding (1)], then the F-HS can be chosen larger than $(k_0\sqrt{\varepsilon_{\max}\mu_{\max}})^{-1}$, thereby concentrating the relevant spectral range near $\sqrt{\varepsilon_{\max}\mu_{\max}}$.

The considerations above imply that the error of the effective formulation is controlled via (6) and (10) by the *dimensionless* scale parameter defined as

$$N_\nu \equiv k_0 K(\xi) \bar{d} 2^{-\nu} \tag{11a}$$

$$\leq 2^{-(\nu-j)} = \frac{\text{M–HS}}{\text{F–HS}} \ll 1 \tag{11b}$$

where, referring to (9), (11a) expresses N_ν as the ratio between the M-HS and the scale of variations of the field, for a given ξ, while (11b) is a bound on N_ν that follows from (10) and applies to the entire relevant wavenumber spectrum.

The quality assessment can be systematized by examining the difference in $\mathbb{V}_j$ between the actual *source-excited* field solution and the solution of the effective formulation, formalized in terms of the nondimensional estimator $\mathcal{E}_j$, which yields the spectral domain error bounds (see [28])

$$\mathcal{E}_j \equiv \frac{\|\mathcal{P}_j V^{\text{ef}} - \mathcal{P}_j V\|}{\|\mathcal{P}_j V^{\text{ef}}\|} \sim k_0 K d N_\nu^2 M_\nu^2 \tag{12a}$$

$$\leq 2^j \left(\frac{d}{\bar{d}}\right) 2^{-2(\nu-j)} M_\nu^2 \tag{12b}$$

where M_ν is defined below and d is the thickness of the laminate. Here and elsewhere the symbol $\|\cdot\|$ denotes the conventional $\mathbb{L}_2[0,d]$ norm via $\|f\| = (\int_0^d |f|^2 dz)^{1/2}$ (note that the functions on the left-hand side of (12a) are in $\mathbb{V}_j \subset \mathbb{L}_2$, whence the norm is in fact in $\mathbb{V}_j$). While (12) is expressed in terms of V, the estimator $\mathcal{E}_j$ for I is the same. The bound in (12b), which follows from (12a) via (10), is a *global* bound for the entire *relevant* spectrum, as defined in (10).

In addition to the small parameter N_ν in (12), which quantifies the ratio between the F-HS and the M-HS, $\mathcal{E}_j$ in (12) also depends on norms of the neglected detailed parts of the medium heterogeneity assembled into the *nondimensional* parameter [28]

$$M_\nu^2 = \frac{\|q^d\|^2}{\|q^{\text{ef}}\|^2} + \frac{\|p^d\|^2}{\|p^{\text{ef}}\|^2} \tag{13}$$

where $\|q^{\text{ef}}\|$ and $\|p^{\text{ef}}\|$ refer only to the norm of the effective medium within the slab region where q^d and/or p^d contribute (i.e., not to the entire z-domain).

Note that the MRH is *not* a perturbation theory valid for weak micro-heterogeneities (small M_ν) since $\mathcal{E}_j$ in (12) is controlled also by the small parameter N_ν^2, which can be made as small as required by increasing ν. Equation (11b) explains the reason for choosing different scales for the medium homogenization (M-HS) and for testing the field (F-HS) since this introduces a built-in small parameter that controls the error.

Finally, as expected, the bound $\mathcal{E}_j$ in (12) on the *source-excited* V solution fails for ξ close to a modal eigenvalue. This limitation, however, does not imply that the effective formulation is invalid for $\xi \simeq \xi_l$ (l is the mode index); it has been

shown that the actual eigenvalues and eigenfunctions are well described by their effective counterparts [25], [26]. Thus the field solutions there can be modeled in terms of the effective eigenfunctions [see also (24)]. The region around the eigenvalues where the bound in (12) is invalid is found in [28] to be

$$\Delta_l \sim \frac{K}{(\xi_l k_0 d)}. \tag{14}$$

In summary, we note the role of the individual homogenization parameters on the required smallness of the overall nondimensional error estimator $\mathcal{E}_j$ in (12). Increasing ν for a given k_0 reduces M_ν and therefore $\mathcal{E}_j$, but this reduction is overpowered by that due to N_ν^2, which behaves like $2^{-2\nu}$ [see (11)]. For a constant ν, on the other hand, the error behaves like k_0^3, as one infers from (12a) using N_ν from (11a). If, however, ν is changed with k_0 such that N_ν in (11a) is constant [i.e., the M-HS in (6) decreases as $k_0 K$ in (11a) increases], then $\mathcal{E}_j$ varies linearly (with the electrical width $k_0 K d$ of the laminate). These trends are substantiated in the numerical examples of Section VI and in Figs. 5–Fig. 7.

This completes the review of the MRH techniques for the formulation of the effective field and medium parameterizations, which are required for the tasks that follow.

C. Derivation of the MRH Via Integral Equation Formulation of the TL Problem

The effective formulation for the spectral domain GF has been defined in terms of the TL equations in (4) and has been discussed in Section III-B1, together with the related error bounds that are found via multiresolution decomposition of the TL equations and field constituents with as yet unspecified boundary conditions. Implementation and justification of this procedure requires the projection of these equations onto $\mathbb{V}_j$. This is best addressed by recasting (4) in an integral equation form since: 1) the integral operator is continuous and 2) the boundary conditions are implicitly included in the kernel, whence the homogenization procedure yields not only the effective μ, ϵ parameters but also the *effective boundary conditions* in the macro-scale formulation [25], [26]. This strategy has been implemented in [28, Sec. 5.1] via a *two-step* procedure wherein each step addresses the effect of only one of the heterogeneity functions p and q (however, see [31] for the derivation of the MRD homogenization directly from the differential wave operator). In the summary below, we consider only one function, say, q.

1) The Integral Equation: An integral equation is obtained by decomposing p, q into the *background* (smooth) and *foreground* (detail) components defined in (7), using the effective smooth components p^{ef}, $q^{\mathrm{ef}} \in \mathbb{V}_M$ as the background. This leads to *two coupled* Lippmann–Schwinger type integral equations [28] wherein the *foreground* components p^d, q^d act as *induced sources* in conjunction with the *dyadic Green's function* for the background. As mentioned above, for simplicity, we assume here that there are only q-type micro heterogeneities. Starting with the known background GF $g^{\mathrm{ef}}_{V_\imath}(z,z')$ which is the V-type response in (4) at z to an $\imath$-type delta function source ($\upsilon = 0$, $\imath = \delta(z-z')/ik_0$) at z' in a smooth background

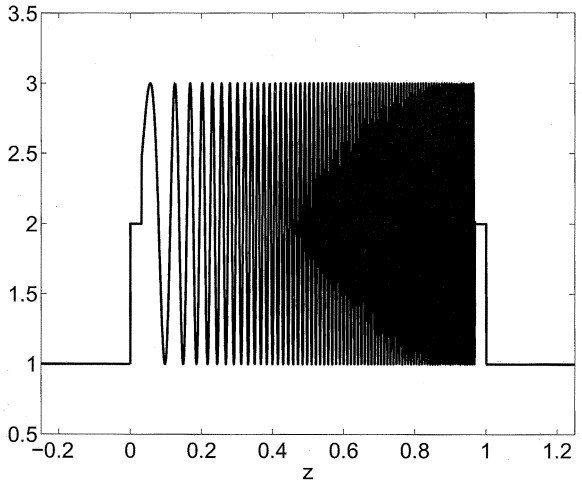

Fig. 3. Heterogeneous permittivity $\varepsilon(z) = 2(1 + \sin(160\pi z^2))$ corresponding to the medium in (33), characterized by a continuous narrowly spaced distribution of the resolutions.

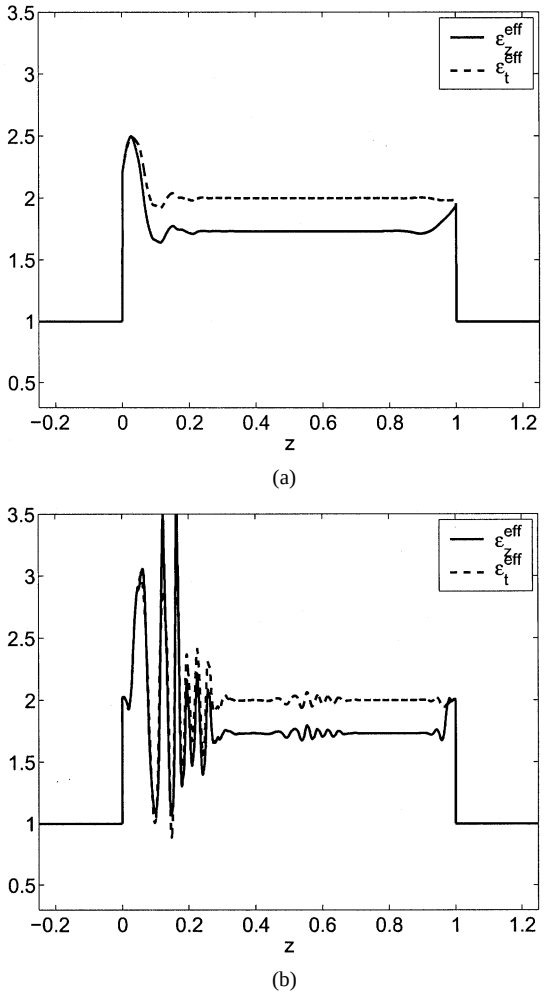

Fig. 4. Effective permittivity for the medium in Fig. 3 using M-HS with (a) $\nu = M = 4$ and (b) finer resolution scale $\nu = M = 6$. Note the effective anisotropy: $\varepsilon_t^{\mathrm{ef}} \neq \varepsilon_z^{\mathrm{ef}}$ (dashed and solid curves, respectively).

$(p,q) = (p^{\mathrm{ef}}, q^{\mathrm{ef}})$, the integral equation for V in a medium with $p = p^{\mathrm{ef}}$ but $q = q^{\mathrm{ef}} + q^d$ is given symbolically by

$$V = F + k_0^2 \mathcal{G}^{\mathrm{ef}}_{V_\imath}\{q^d V\}. \tag{15}$$

Here, the integral operator is defined by $\mathcal{G}^{\rm ef}_{V_\imath}\{f(z)\} = \int_0^d g^{\rm ef}_{V_\imath}(z,z')f(z')dz'$, and the forcing term is given by $F = ik_0(\mathcal{G}^{\rm ef}_{I_\imath}\{\imath\} + \mathcal{G}^{\rm ef}_{I_\upsilon}\{\upsilon\})$, where $\mathcal{G}^{\rm ef}_{I_\imath}$ is defined in a similar fashion but for the I-type response to an $\imath$-type source.

2) Multiresolution Decomposition of the Integral Equation: We proceed by expressing $V = V^s + V^d$ in terms of its smooth and detail components in accord with (A4) and (A5), and then take the inner product of (15) with the sets of scaling (ϕ) and wavelet (ψ) basis functions, thereby reducing (15) to the algebraic equation

$$\begin{pmatrix} \mathbf{I}-\mathbf{\Phi}^q & -\mathbf{C}^q \\ -\bar{\mathbf{C}}^q & \mathbf{I}-\mathbf{\Psi}^q \end{pmatrix} \begin{pmatrix} \boldsymbol{s}^q \\ \boldsymbol{d}^q \end{pmatrix} = \begin{pmatrix} \boldsymbol{s}^{\rm ef} \\ \boldsymbol{d}^{\rm ef} \end{pmatrix}. \tag{16}$$

Here, the unknown vectors $\boldsymbol{s}^q$ and $\boldsymbol{d}^q$ represent the smooth and detail *expansion coefficients* of V, while the known vectors $\boldsymbol{s}^{\rm ef}$ and $\boldsymbol{d}^{\rm ef}$ are the corresponding expansion coefficients of F in (15). The elements of the matrices $\mathbf{\Phi}$, $\mathbf{C}$, $\bar{\mathbf{C}}$ and $\mathbf{\Psi}$, which describe the MRD of the integral operator, are defined by the projections

$$[\Phi^q]_{n,n'} = k_0^2 \left\langle \phi_{jn}, \mathcal{G}^{\rm ef}_{V_\imath}\{q^d \phi_{jn'}\}\right\rangle \tag{17a}$$
$$[C^q]_{n,m'n'} = k_0^2 \left\langle \phi_{jn}, \mathcal{G}^{\rm ef}_{V_\imath}\{q^d \psi_{m'n'}\}\right\rangle \tag{17b}$$
$$[\bar{C}^q]_{mn,n'} = k_0^2 \left\langle \psi_{mn}, \mathcal{G}^{\rm ef}_{V_\imath}\{q^d \phi_{jn'}\}\right\rangle \tag{17c}$$
$$[\Psi^q]_{mn,m'n'} = k_0^2 \left\langle \psi_{mn}, \mathcal{G}^{\rm ef}_{V_\imath}\{q^d \psi_{m'n'}\}\right\rangle \tag{17d}$$

where $\mathbf{I}$ is the identity matrix. Note that $\langle f, g\rangle = \int_0^d f(z)g(z)dz$ is not an inner product (in the sense of metric spaces), but this definition of the matrices is typically used in Galerkin-type projection of integral equations [35]. The properties of the matrices in (17) are explored in [28, Sec. 6.1], by analyzing the properties of the known effective medium operator $\mathcal{G}^{\rm ef}_{V_\imath}$.

The smooth/detail decomposition in (16) is exact and formally assigns equal importance to the "s" and "d" constituents. Since we are interested in an effective smooth-scale formulation, we eliminate $\boldsymbol{d}^q$ by solving for it from the second equation in (16) and substituting into the first equation to obtain

$$\left[\mathbf{I} - \underbrace{\left(\mathbf{\Phi}^q + \mathbf{C}^q(\mathbf{I}-\mathbf{\Psi}^q)^{-1}\bar{\mathbf{C}}^q\right)}_{\mathbf{EMO}^q}\right] \boldsymbol{s}^q = \boldsymbol{s}^{\rm ef} + \mathbf{C}^q(\mathbf{I}-\mathbf{\Psi}^q)^{-1}\boldsymbol{d}^{\rm ef}. \tag{18}$$

The "effective material operator" $\mathbf{EMO}^q$ in (18) incorporates the effects of the detail scales within the smooth-scale equation (we use the superscript q to identify the special case where there is only q-type micro heterogeneity). The second term on the right-hand side in (18) represents the coupling of the micro scales in the forcing term $\boldsymbol{d}^{\rm ef}$ into the macro-scale field $\boldsymbol{s}^q$ via the medium micro-heterogeneities; since the source functions υ and $\imath$ represent physical sources they are typically smooth, whence F in (15) is also smooth and the norm $\|\boldsymbol{d}^{\rm ef}\| \approx 0$. Solving the thus reduced equation (18) for $\boldsymbol{s}^q$ requires the inverse "operation" $(\mathbf{I} - \mathbf{EMO}^q)^{-1}$. Since our goal is to approximate $\boldsymbol{s}^q$ by $\boldsymbol{s}^{\rm ef}$, the norm $\|\mathbf{EMO}^q\|$ should be small. Choosing the problem parameters accordingly, the first-order Neumann series solution of (18) becomes, using $(\mathbf{I} - \mathbf{EMO}^q)^{-1} \sim \mathbf{EMO}^q$

$$\boldsymbol{s}^q \approx \boldsymbol{s}^{\rm ef} + \mathbf{EMO}^q \boldsymbol{s}^{\rm ef} \tag{19}$$

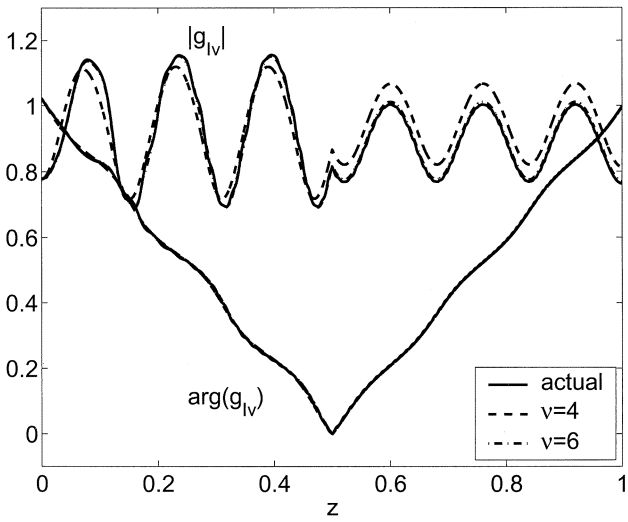

Fig. 5. Spectral Green's function $g^e_{I_v}$ for a source at $z' = 0.5$ with frequency $k_0 = 15$, $d = 1$, and for the spectral parameter $\xi = 0.5$. The curves are shown for $|g_{Iv}|$ multiplied by 20 and $\arg\{g_{Iv}\}$ divided by ten. The solid, dashed, and dashed-dotted curves correspond to the actual solution and to the effective solutions for $\nu = 4$ and 6, respectively. (See discussion in Section VI-B.)

with the error estimate $\|\boldsymbol{s}^q - \boldsymbol{s}^{\rm ef}\|/\|\boldsymbol{s}^{\rm ef}\| \sim \|\mathbf{EMO}^q\|$. Thus, the bound on the error may be calculated readily from the bound on the matrices that form the $\mathbf{EMO}$ in (18).

This brings us back to Section III-B2 and the quality assessment of the effective formulation in (12). Although the error bound in (12) applies to the more general case where there are both q and p micro heterogeneities, it also applies to the present case by using only the q-part of M_ν in (13), i.e., $M^q_\nu = \|q^d\|/\|q^{\rm ef}\|$. Comparing the error bounds in (12) with those from (19), one concludes that $\mathcal{E}_j \sim \|\mathbf{EMO}^q\|$ and that $\|\mathbf{EMO}^q\|$ is quantified by the expression on the right-hand side of (12). As in the discussion following (13), we assume here that ξ is sufficiently removed from the modal eigenvalues ξ_l; otherwise the $\mathbf{EMO}^q$ is unbounded. In that case, the solution can be obtained in terms of the source-free eigenfunctions [29].

IV. Spectral Equivalence for the Actual and Effective Fields

A. Characteristic Green's Functions and the Spectral Completeness Relations

The z-domain wavenumber spectrum of the wave equation plays an important role in guided wave theory, where it is often advantageous to describe the source-excited field in terms of the spectrum of the z-domain eigenfunctions. Following [6, Sec. 3.3] and [39], the z-domain spectral problem will be discussed from the fundamental perspective of its *characteristic Green's functions*, which are defined in the *complex* spectral domain.

As discussed in Section III-A, the complete source-excited vector field solution involves a discrete and/or continuous summation over the transverse E- and H-type vector modes, identified by the superscript $\alpha = e$ and h, respectively. The modal field amplitudes (V^α, I^α) are described by solutions of the z-domain spectral TL equations, excited by sources whose amplitudes (v^α, i^α) are obtained by projecting the actual vector current distribution onto the modal eigenfunctions. Referring

to [6, Sec. 2.3c], the most general solution of the TL problem can be expressed in terms of the characteristic GF $g^{\alpha}_{A,b}(z,z';\xi)$, which expresses the V^{α} or I^{α} response at z due to a v^{α} or $\imath^{\alpha}$-type impulsive source $\delta(z-z')/ik_0$ at z' [e.g., g^{e}_{Iv} is an I-type solution of (4) for an E-type mode with a $v^{e}(z)=\delta(z-z')/ik_0$ excitation; this notation has already been used in connection with (15)]. It is sufficient to solve only for the fundamental functions g^{e}_{Iv} and $g^{h}_{V\imath}$ since they determine the solutions due to all other types of excitations via reciprocity. From (4) and (5), we obtain the *Sturm–Liouville* equation for $g^{e}_{Iv}(z,z';\xi)$

$$\left[\frac{d}{dz}\frac{1}{q^{e}}\frac{d}{dz}+k_0^2p^{e}\right]g^{e}_{Iv}=\left[\frac{d}{dz}\frac{1}{\varepsilon_t}\frac{d}{dz}+k_0^2\left(\mu_t+\frac{\lambda}{\varepsilon_z}\right)\right]g^{e}_{Iv}=-\delta(z-z') \tag{20}$$

where λ is a spectral parameter in the complex λ-plane that is related to $\boldsymbol{\xi}$ in Section III via $\xi^2=\boldsymbol{\xi}\cdot\boldsymbol{\xi}=-\lambda$. The equation for $g^{h}_{V\imath}$ is given by (20) with $\mu\leftrightarrow\varepsilon$. Henceforth we shall only consider the E-type Green's function and omit the indexes; i.e., $g^{e}_{Iv}\equiv g$. The H-type solutions can be analyzed in a similar fashion.

The boundary conditions (BCs) that are satisfied by g and are therefore imposed on the solutions of the corresponding TL equations are dictated by the ambient physical problem environment (recall that g is an I- or a V-type solution for E or H modes, respectively). The "basic" BC is that for an infinitely extended medium along the propagation coordinate [chosen as z in (20)], which translates in the spectral domain into the "radiative" (outgoing wave) condition for TL modal fields (V^{α}, I^{α}) excited by actual or induced modal sources (v^{α}, $\imath^{\alpha}$). However, other types of Green's functions that satisfy different boundary conditions can be constructed by adding to the basic solutions, denoted by g, any *source-free* solution of the Sturm–Liouville equation (20), which renders the result better adapted to other problem environments. Examples may involve smooth and abrupt (junction) inhomogeneities along the TL propagation coordinate, cascaded and terminated geometries, etc., where appropriately modified BCs on the conglomerate TL equations can be matched self-consistently (via a comprehensive field-network architecture) to alternative network formulations for complex systems of transmission lines (media) that are connected at one or more terminals (interfaces) [36]–[38] (see Part II [34]).

Returning to (20), the basic solution is given formally by [6, Sec. 3.3b]

$$g(z,z';\lambda)=\frac{\overleftarrow{V}(z_<)\overrightarrow{V}(z_>)}{\varepsilon_t^{-1}W(\overleftarrow{V},\overrightarrow{V})}$$
$$W(\overleftarrow{V},\overrightarrow{V})=\left(\overrightarrow{V}\frac{d\overleftarrow{V}}{dz}-\overleftarrow{V}\frac{d\overrightarrow{V}}{dz}\right) \tag{21}$$

where $z_<$ and $z_>$ denote the smaller and larger values of z and z', respectively, $\overleftarrow{\overrightarrow{V}}$ are source-free solutions that satisfy the basic radiative boundary conditions on the left- and right-hand sides of the propagation medium, and W is the Wronskian. The

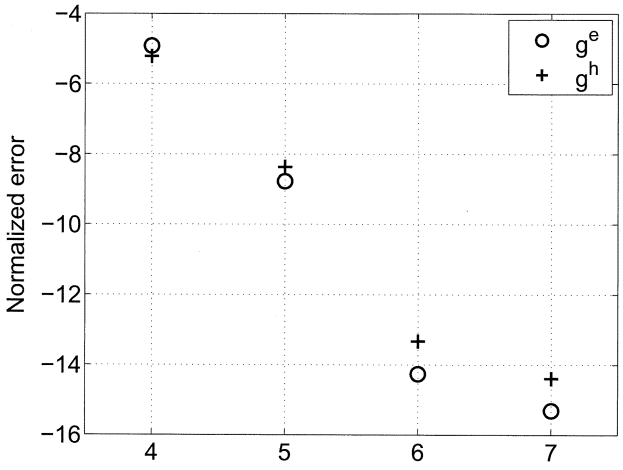

Fig. 6. Normalized error estimator $\mathcal{E}_j\ \bar{M}^2_{\nu=4}/\bar{M}^2_{\nu}$ in (12) (see text for an explanation of the normalization) is plotted on a $\log_2$ scale as a function of the M-HS index ν for the effective GFs g^{e}_{Iv} and $g^{h}_{V\imath}$. The medium is shown in Figs. 3 and 4. Problem parameters (see Fig. 5): $k_0=15$, $d=1$ and $z'=-0.1$, $\xi=0.5$. (See discussion in Section VI-B.)

radiative GF is employed in this paper in the example in Section V-B. To construct a network representation for the radiative TL problem, one selects a set of left and right "modal terminals" far from a central reference place. Augmenting the *outgoing* "scattered" *secondary* fields at these terminals by *ingoing primary* excitation leads to a *scattering matrix* network description matched to the modal g. Alternatively, by *adding* to the *ingoing* propagating mode fields at the TL terminals, the corresponding *outgoing* propagating fields that satisfy the source-free TL equations, one generates *standing wave* BCs that define the "reactive" TL-GF g^{α}_{R} with its corresponding *impedance/admittance matrix* network representations. Finally, by *subtracting* from g^{α} its *left-propagating* source-free mode portion, one generates a *right-radiating unidirectional* TL-GF $\overrightarrow{g}^{\alpha}$. Together with its unidirectional *left-radiating* counterpart $\overleftarrow{g}^{\alpha}$, these TL-GFs define a *transfer matrix* network description that is well adapted to cascaded configurations. These aspects are explored in detail in Part II [34].

For any of the above boundary conditions, the characteristic Green's functions generate the complete spectrum of equations (20) via the completeness theorem [6, Ch. 3.3], [39]

$$\varepsilon_z(z)\delta(z-z')=\frac{k_0^2}{2\pi i}\oint_{\mathcal{C}_\lambda}d\lambda g(z,z';\lambda) \tag{22a}$$
$$=\sum_{l}U_l(z)U^{*}_{\ell}(z')+\int_{\mathcal{B}^{+}}d\lambda U(z;\lambda)U^{*}(z';\lambda) \tag{22b}$$

where the asterisk denotes complex conjugation. In (22a), the integration contour $\mathcal{C}_\lambda$ at $|\lambda|\to\infty$ encloses in the positive sense the entire upper Riemann sheet of the generally multisheeted complex λ-plane (see Fig. 8). Using Jordan's lemma and Cauchy's theorem, (22b) is obtained by deforming the integration contour around the pole and branch point singularities on the upper Riemann sheet [where $\mathrm{Im}\sqrt{\lambda+1}\geq 0$; see (20)], and invoking the residue theorem plus branch cut integration.

Thus, the first term in (22b) is a summation over the *discrete* eigenfunctions $U_l(z)$, which represent the

residue contributions from the poles λ_l of g such that $U_l(z)U_l^*(z') = \text{res}[k_0^2 g(z,z';\lambda)]_{\lambda_l}$. The second term in (22b) represents the contribution of the continuous spectrum, obtained by integrating around the branch cut of g in the λ plane and symmetrizing the integrand. Assuming, for example, that $\varepsilon = \mu = 1$ outside the slab, the branch cut extends from $\lambda = -1$ to $+\infty$ along the real λ axis. The integration contour $\mathcal{B}^+$ follows the side of the cut whereon $\text{Im}\{\lambda\} = i0^+$ (i.e, the upper half of $\mathcal{B}$ in Fig. 8. For details, see [6, ch. 3.3].

The spectral theorem for the *effective* problem is given by (22) with the replacements

$$g \to g^{\text{ef}}, \quad U_l \to U_l^{\text{ef}}, \quad \varepsilon_{t,z}, \mu_{t,z} \to \varepsilon_{t,z}^{\text{ef}}, \quad \mu_{t,z}^{\text{ef}}. \tag{23}$$

B. Quality Assessment of the Actual-Effective Spectral Equivalence

As before, it is important to establish the desired equivalence between the spectra of the actual and effective formulations in the observables space $\mathbb{V}_j$. The spectral expansions in $\mathbb{V}_j$ are obtained by projecting (22) onto $\mathbb{V}_j$ via the smoothing operator $\mathcal{P}_j$ in (A5a), applied with respect to both the z and the z' coordinates. This practically annihilates the contribution from what will be termed the "irrelevant spectral range" $|\lambda| > \lambda_j$, wherein g is a rapidly varying function of z and hence yields vanishing contributions in the projection. Thus, shrinking the integration contour $\mathcal{C}_\infty$ in (22) to $\mathcal{C}_{\lambda_j}$ that encircles only the "relevant" regime (to be defined later; see Fig. 8), and combining the contributions outside $\mathcal{C}_{\lambda_j}$ in a remainder R_j, we are led to the following "smooth-space expansions" for the actual problem

$$\mathcal{P}_j\{\varepsilon_z(z)\delta_j(z,z')\} = \frac{k_0^2}{2\pi i}\oint_{\mathcal{C}_{\lambda_j}} \mathcal{P}_j\mathcal{P}_j' g(z,z';\lambda)d\lambda + R_j \tag{24a}$$

$$= \sum_{l=0}^{l_j} \mathcal{P}_j U_l(z)\mathcal{P}_j' [U_l(z')]^* + \int_{\mathcal{B}_j^+} d\lambda \mathcal{P}_j U(z,\lambda) \times \mathcal{P}_j' [U(z',\lambda)]^* + R_j. \tag{24b}$$

The function $\delta_j(z,z') \equiv \mathcal{P}_j'\delta(z-z') = \sum_n \phi_{jn}(z')\phi_{jn}(z)$ is the canonical "point source" for the homogenized formulation, obtained by projecting $\delta(z-z')$ onto $\mathbb{V}_j$. The first term in (24b) is a summation over l_j discrete "relevant modes," while the second term represents the "relevant continuous (radiation) spectrum" defined over the relevant part of the branch cut $\mathcal{B}_j$ (see Fig. 8; $\mathcal{B}^+$ follows the side of the cut whereon $Im\lambda = io^+$). The remainder R_j expresses the contributions of the irrelevant spectrum outside $\mathcal{C}_{\lambda_j}$. A bound on R_j is given in [29]; it is parameterized by λ_j, which identifies the location on the real λ axis of the highest order mode included in the "relevant spectral range." For a given choice of the F-HS, λ_j should be chosen such that R_j is negligible relative to $|\delta_j|$, which is $O(2^j\bar{d}^{-1})$. As an example, consider the case discussed in connection with (1), where the F–HS $\simeq (k_0\sqrt{\varepsilon_{\max}\mu_{\max}})^{-1}$ is chosen according to the shortest wavelength in the medium. One finds that $\lambda_j \gtrsim \varepsilon_{\max}^{\text{ef}}\mu_{\max}^{\text{ef}} - \varepsilon_{\min}^{\text{ef}}\mu_{\min}^{\text{ef}} > 0$; the relevant spectrum consists of all discrete (trapped) modes and a portion of the continuous spectrum (this case is schematized in Fig. 8). For details, see [29, see 4.2].

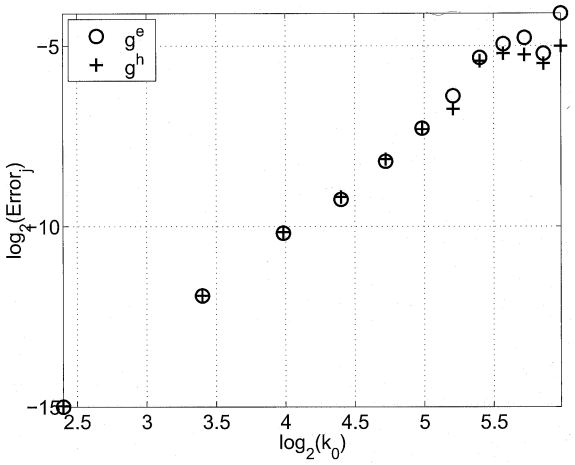

Fig. 7. As in Fig. 6 but for $\mathcal{E}_j$ as a function of k_0 with constant ν. With $\nu = 8$, the M-HS is chosen fine enough to validate the effective formulation over the entire relevant frequency spectrum. (See discussion in Section VI-B.)

The expressions for the corresponding effective problem are the same as (24), with the replacements in (23). It has also been shown in [29] that the spectral constituents of the actual and effective problems are equivalent up to a given error, which is bounded by

$$\frac{\left\|\mathcal{P}_j U_l - \mathcal{P}_j U_l^{\text{ef}}\right\|}{\left\|\mathcal{P}_j U_l^{\text{ef}}\right\|} \sim \|\mathbf{EMO}\| \sim k_0 K d N_\nu^2 M_\nu^2 \le 2^j \left(\frac{d}{\bar{d}}\right) 2^{-2(\nu-j)} M_\nu^2 \tag{25a}$$

$$\left|\lambda_l - \lambda_l^{\text{ef}}\right| \sim K^2 N_\nu^2 M_\nu^2 \le k_0^{-2}\bar{d}^{-2}2^{2j}2^{-2(\nu-j)}M_\nu^2 \tag{25b}$$

where λ_l, U_l and $\lambda_l^{\text{ef}}, U_l^{\text{ef}}$ are the eigenvalues and eigenfunctions of the actual and effective problems. The various parameters in (25) are defined and discussed in (12) and (13) (see also [28, Sec. 3.3]). Note, that the error bound (25a) for *modal* fields at the eigenvalues is the same as in (12) for the *source-excited* fields far enough from these eigenvalues, as specified in (14). (For the proof of (25), see [29, Sec. 5]). Numerical examples are provided in Section VI-C and in Figs. 9 and 10.

V. Spectral Synthesis and Quality Assessment of the 3-D Effective Scalar Green's Functions

Having completed and "calibrated" the actual-effective field formulation in the 1-D z-domain spectral regime, we can now return to Section III-A for spectral synthesis of the 3-D effective total vector field. It is well known that the 3-D dyadic GFs excited by arbitrarily oriented electric or magnetic dipoles can be constructed in terms of E-type and H-type scalar GFs [6, ch. 7.2]. To highlight relevant issues pertaining to implementation of the theory for the 3-D effective field in a simple format, we consider the special case of excitation by a vertically polarized electric current source $\mathbf{J} = \hat{\mathbf{z}}J_0\delta(\mathbf{r}-\mathbf{r}')$ [see Figs. 1(b), 11(a), or 12(a) with the source located either inside or outside the laminate], which permits the 3-D vector field in the presence of the

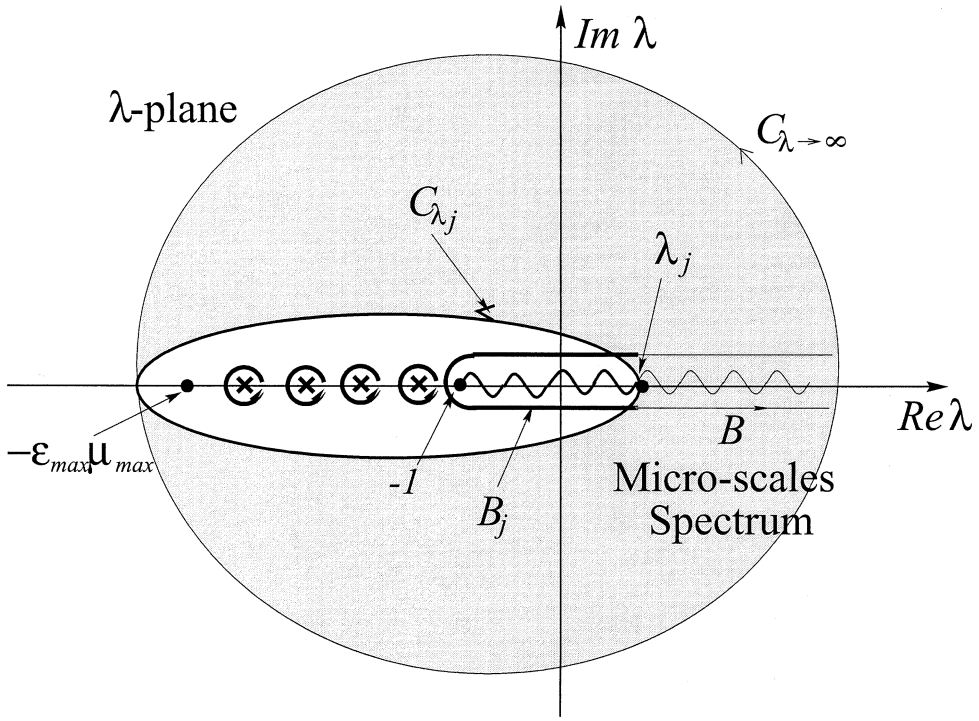

Fig. 8. Relevant (unshaded) and nonrelevant (shaded) regimes in the complex spectral λ-plane. The corresponding physical configuration is that of Fig. 1(b). The spectral contour $\mathcal{C}_{\lambda_j}$ encircles only the "relevant" spectral domain; the exterior "nonrelevant" $\mathcal{C}_{\lambda_j}$ is parameterized by its point of intersection with the largest spectral pole λ_j on the real axis [see discussion after (24)]. $\otimes$: spectral poles λ_l located on the real axis segment $-\sqrt{\mu_{\max}\varepsilon_{\max}} < \lambda < -1$. Wiggly line: branch cut extending from the branch point at $\lambda = -1$ along the real axis segment $\lambda > -1$. B and B_j: the complete and "relevant" branch-cut integration contours, respectively.

complex laminate to be fully described by the E-type scalar potential. The corresponding E-mode Green's function $G^e(\mathbf{r},\mathbf{r}')$ is defined by

$$\left[\frac{\partial}{\partial z}\frac{1}{\varepsilon_t}\frac{\partial}{\partial z}+\frac{1}{\varepsilon_z}\nabla_t^2+k_0^2\mu_t\right]G^e(\mathbf{r},\mathbf{r}')=-\delta(\mathbf{r}-\mathbf{r}') \quad (26)$$

where $\nabla_t^2=\partial_x^2+\partial_y^2$. Once G^e is found (and properly parameterized), the total vector electromagnetic field can be found via [6, ch. 7.2c], [29]

$$\begin{pmatrix}\mathbf{H}(\mathbf{r},\mathbf{r}')\\ \mathbf{E}_t(\mathbf{r},\mathbf{r}')\\ E_z(\mathbf{r},\mathbf{r})\end{pmatrix}=J_0\begin{pmatrix}\varepsilon_z^{-1}(z')\nabla\times\hat{\mathbf{z}}\\ \left(\frac{\eta}{ik_0}\right)\varepsilon_t^{-1}(z)\varepsilon_z^{-1}(z')\partial_z\nabla_t\\ -\left(\frac{\eta}{ik_0}\right)\varepsilon_z^{-1}(z)\varepsilon_z^{-1}(z')\nabla_t^2\end{pmatrix}G^e(\mathbf{r},\mathbf{r}'). \quad (27)$$

We shall henceforth omit the superscript e. The field in the *effective* medium is described by the same formulation except that the medium coefficients $\varepsilon_{t,z}$ and $\mu_{t,z}$ are replaced by the effective coefficients in (8). The effective observables are then obtained by smoothing these fields with respect to both z and z'.

Although the original 3-D vector field decomposition in Section III-A was performed in terms of transverse vector eigenfunctions with propagation along z, the use of characteristic Greens's functions in the *complex* spectral domain permits selection of propagation along any of the three coordinate directions, with eigenmodes defined in the remaining 2-D cross-sections [6, ch. 3]. Two such alternative representations are shown in SectionsV-A and V-B below. They exhibit entirely different phenomenologies, with different parameterizations of the same 3-D vector field. Either of them can be derived from generalized characteristic GFs set in the three complex wavenumber spectral domains corresponding to the three physical coordinates [6, ch. 3].

A. Transverse Eigenfunction Expansion: z Propagation

The 3-D effective field in the z-propagation representation can be found in terms of the scalar counterpart of the vector transverse mode expansion in Section III-A

$$G^{\rm ef}(\mathbf{r},\mathbf{r}')=\sum_{\boldsymbol{\xi}}\Phi(\boldsymbol{\rho},\boldsymbol{\xi})\Phi^*(\boldsymbol{\rho}',\boldsymbol{\xi})g^{\rm ef}(z,z';\lambda=-\xi^2) \quad (28)$$

where $\Phi(\boldsymbol{\rho},\boldsymbol{\xi})$ are the E-type scalar mode functions corresponding to the transverse spectral parameter $\boldsymbol{\xi}=(\xi_x,\xi_y)$ and $g^{\rm ef}$ is the effective GFs corresponding to $\lambda=-\xi^2\equiv-\boldsymbol{\xi}\cdot\boldsymbol{\xi}$. For the case of unbounded transverse cross-sections, (28) becomes [6]

$$G^{\rm ef}(\mathbf{r},\mathbf{r}')=\frac{k_0^2}{4\pi^2}\int d^2\xi\, e^{ik_0\boldsymbol{\xi}\cdot(\boldsymbol{\rho}-\boldsymbol{\rho}')}g^{\rm ef}(z,z';\lambda=-\xi^2) \quad (29)$$

where $g^{\rm ef}(z,z';\lambda)$ is defined by (20) and is given formally by [see (21)]

$$g^{\rm ef}(z,z';\lambda)=\frac{\overleftarrow{V}^{\rm ef}(z_<)\overrightarrow{V}^{\rm ef}(z_>)}{\left(\varepsilon_t^{\rm ef}\right)^{-1}W^{\rm ef}(\overleftarrow{V}^{\rm ef},\overrightarrow{V}^{\rm ef})}$$

$$W^{\rm ef}(\overleftarrow{V}^{\rm ef},\overrightarrow{V}^{\rm ef})=\overrightarrow{V}^{\rm ef}\frac{d\overleftarrow{V}^{\rm ef}}{dz}-\overleftarrow{V}^{\rm ef}\frac{d\overrightarrow{V}^{\rm ef}}{dz}. \quad (30)$$

Note that $g^{\rm ef}$ is evanescent for $\xi > \sqrt{\varepsilon^{\rm ef}_{z\,\max}\mu^{\rm ef}_{t\,\max}}$; therefore if $z \neq z'$, the integration can be limited to $\xi < \sqrt{\varepsilon^{\rm ef}_{z\,\max}\mu^{\rm ef}_{t\,\max}}$. The M-HS (medium homogenization scale) will be determined here by requiring the error of the effective formulation to be small in this spectral regime. From (9) K, in this range, is largest for $\xi = 0$ with $K = \sqrt{\varepsilon^{\rm ef}_{\max}\mu^{\rm ef}_{\max}}$, thus implying from (12) that the largest error occurs at $\xi = 0$. Using the first expression in (11a) for N_ν in (12), we obtain the desired value for M-HS$= 2^{-\nu}\bar{d} \sim M_\nu^{-1}(k_0\sqrt{\varepsilon^{\rm ef}_{\max}\mu^{\rm ef}_{\max}})^{-3/2}d^{-1/2}$.

The representation in (28) is convenient for determination of the field away from the source in the vicinity of the z-axis [see Fig. 12(a)], where z-propagation phenomena (with multiple reflections) predominate.

B. z-Domain Eigenfunction Expansion: Transverse Propagation

As noted earlier, the 3-D scalar Green's function can alternatively be calculated as a summation over the eigenfunctions in the z domain, propagating in the lateral (transverse) direction. This guided mode representation is convenient when the source and observer are at laterally separated locations *in* or *near* the inhomogeneous laminate, where transverse propagation phenomena predominate. Using the eigenfunction set in (24b), we obtain

$$G^{\rm ef}(\boldsymbol{r},\boldsymbol{r}') = \sum U_l^{\rm ef}(z)U_l^{\rm ef}(z')g_t\left(\boldsymbol{\rho},\boldsymbol{\rho}';\xi_l^{\rm ef} = \sqrt{-\lambda_l^{\rm ef}}\right) + \int_{\mathcal{B}^+} d\lambda U^{\rm ef}(z;\lambda)U^{{\rm ef}*}(z';\lambda)g_t(\boldsymbol{\rho},\boldsymbol{\rho}';\xi = \sqrt{-\lambda}) \tag{31}$$

where the first and second terms involve the discrete and continuous spectral constituents in the z domain. Applying (22) to the present problem, where the laminate is surrounded by a uniform medium at $z < 0$ and $z > d$, with $\varepsilon = \mu = 1$, we note that the upper Riemann sheet in the complex λ-plane is defined by $\mathrm{Im}\sqrt{1+\lambda} \geq 0$, with a branch cut $\mathcal{B}$ extending from the branch point at $\lambda = -1$ to ∞ along the real axis (see Fig. 8). Following the discussion in (22b), the integration is performed along the side $\mathrm{Im}\lambda > 0$ of $\mathcal{B}$, denoted in (22b) and (31) as $\mathcal{B}^+$. Thus, in (31) we have $\xi > 0$ for that part of $\mathcal{B}^+$ where $\lambda < 0$ and $\xi = i\sqrt{\lambda}$ for the part where $\lambda > 0$. The discrete modes in (31) are generated by possible pole singularities of $g^{\rm ef}$ at $\lambda_l^{\rm ef}$, $l = 1,2\ldots$, which are located (for a lossless medium) along the real axis segment $\lambda \in (-\max_z\{\varepsilon^{\rm ef}\mu^{\rm ef}\}, -1)$ [see (22b)], so that $\xi_l^{\rm ef} > 0$ there.

The lateral propagation of these constituents is described by the known transverse-domain Green function $g_t(\boldsymbol{\rho},\boldsymbol{\rho}';\xi)$ that satisfies $[\nabla_t^2 + k_0^2\xi^2]g_t(\boldsymbol{\rho},\boldsymbol{\rho}';\xi) = -\delta(\boldsymbol{\rho}-\boldsymbol{\rho}')$ with appropriate boundary conditions. For an unbounded transverse domain with its "radiative" (radiation) condition at $\rho \to \infty$, the solution is given by $g_t(\boldsymbol{\rho},\boldsymbol{\rho}';\xi) = (i/4)\,H_0^{(1)}(k_0\xi|\boldsymbol{\rho}-\boldsymbol{\rho}'|)$, where $H_0^{(1)}$ is the Hankel function of the first kind and $\xi = \sqrt{-\lambda}$, with λ denoting the spectral parameter in the z-domain.

In view of the spectral equivalence established in Section IV-B, the effective spectrum representation in (31) provides a good approximation to the Green's function solution of the actual problem. This statement applies as long as the error accumulation of the lateral phase, which arises from errors in the eigenvalues in (31), is small ($< \pi$), i.e.,

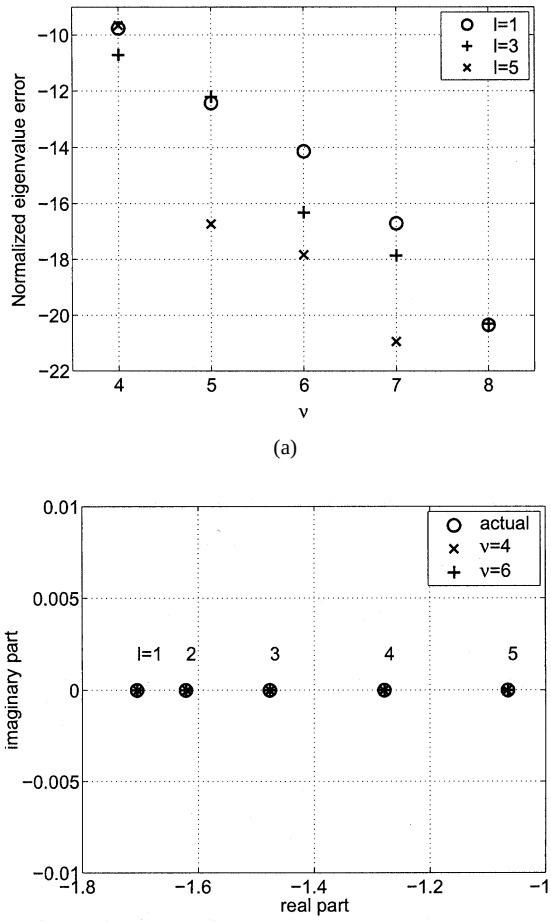

(a)

(b)

Fig. 9. (a) Eigenvalue error $|\lambda_l^{\rm ef} - \lambda_l|$ for $l = 1, 3,$ and 5 modes, normalized by $\bar{M}^2_{\nu=4}/\bar{M}^2_\nu$ (see text), is shown on a $\log_2$ scale as a function of the M-HS scale index ν. (b) λ_l and $\lambda_l^{\rm ef}$ in the complex λ plane for $\nu = 4$ and 6. (See discussion in Section VI-C.)

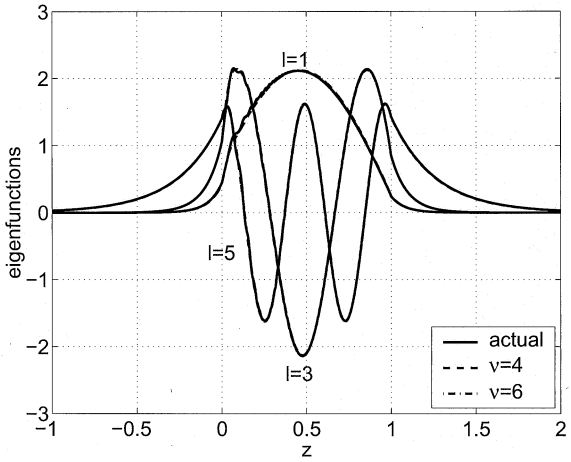

Fig. 10. The ($l = 1, 3,$ and 5) actual and effective modal fields for $\nu = 4$ and $\nu = 6$ as a function of z (solid, dashed, and dashed-dotted curves, respectively). Note the exponential decay outside the laminate slab ($z < 0$ and $z > d = 1$).

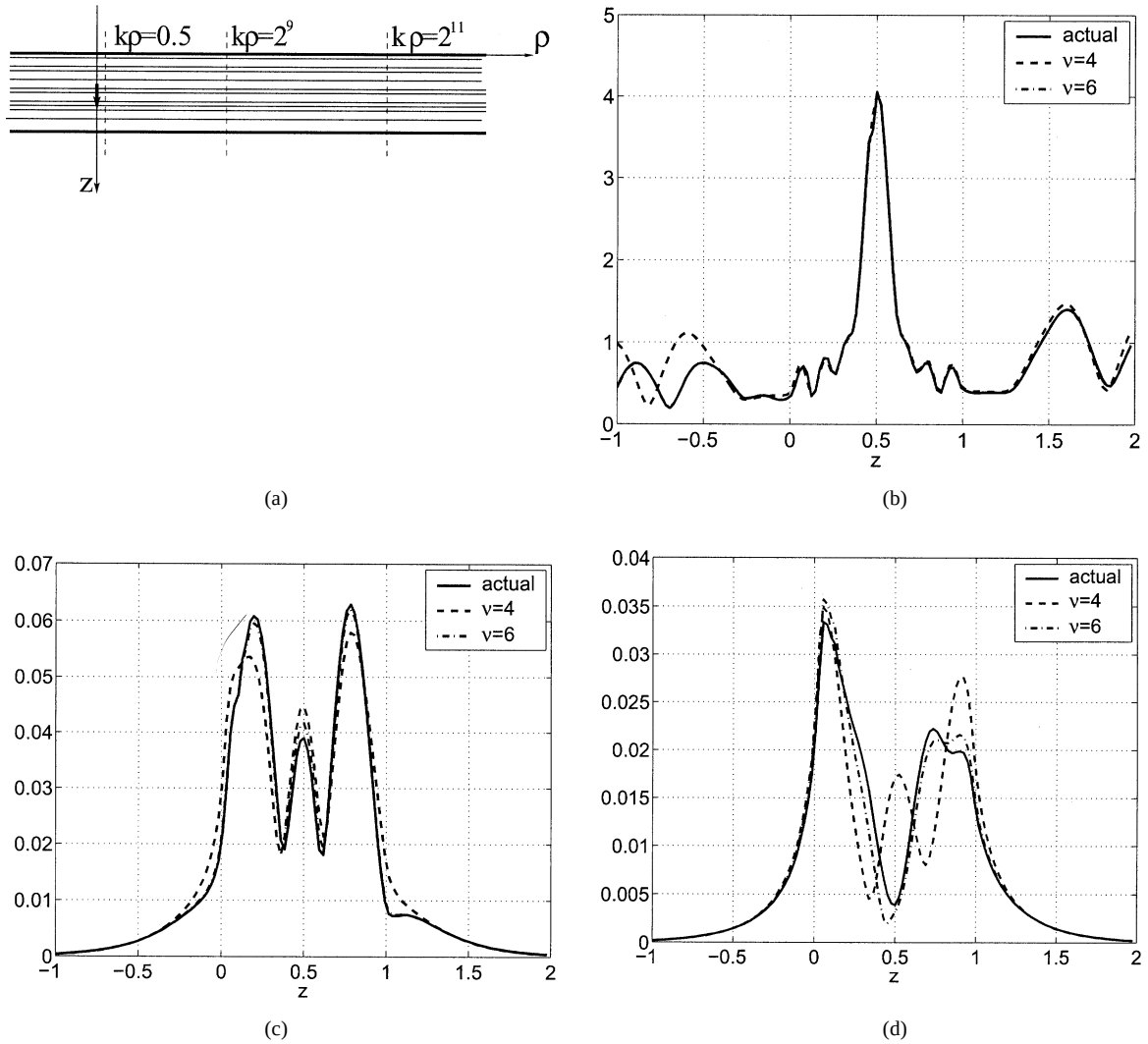

Fig. 11. 3-D Green's function $G(\mathbf{r}, \mathbf{r}')$ within the complex laminate slab for a source located inside the slab at $z' = 0.5$ and $(x', y') = (0, 0)$. (a) Physical configuration. (b), (c), and (d) Cross-sectional cuts of $|G|$ at $k_0\rho = 0.5, 2^9$, and 2^{11}, respectively, where $\rho = |\boldsymbol{\rho}|$ is the lateral displacement. The solid, dashed, and dashed-dotted curves correspond to the actual solution and to the effective solutions for $\nu = 4$ and 6, respectively.

$k_0|\boldsymbol{\rho} - \boldsymbol{\rho}'| \lesssim |\xi_l - \xi_l^{\mathrm{ef}}|^{-1} \sim \xi_l^{\mathrm{ef}}(KN_\nu M_\nu)^{-2}$, where the bound on $|\xi_l - \xi_l^{\mathrm{ef}}|$ is obtained from (25b). This expression is useful if $|\xi_l^{\mathrm{ef}}|$ is not too small; note that this is indeed the case for the dominant laterally propagating modes.

C. Asymptotic Representation: Effective Rays and Effective Leaky Modes

Outside the inhomogeneous region, at distances large compared to the electrical width of the slab, the spectral integral in (29) can be evaluated asymptotically by deforming the original integration contour into the steepest descent path (SDP) through the saddle point ξ_s in the complex ξ-plane. The field is thus described in terms of the saddle point contribution, which is interpreted as the geometrical ray field from the source to the observer, with ξ_s defining the ray direction, plus the contributions of the (real) guided and (complex) leaky wave poles, which are intercepted during the deformation from the original path to the SDP. Since a portion of the SDP passes through the lower (improper) Riemann sheet, the result can be expressed as [6, Sec. 5.6a]

$$G^{\mathrm{ef}}(\mathbf{r}, \mathbf{r}') \sim G^{\mathrm{efsp}}(\mathbf{r}, \mathbf{r}') + \sum_{l=1}^{L} G_l^{\mathrm{efg}}(\mathbf{r}, \mathbf{r}') + \sum_{l'=1}^{L'} G_{l'}^{\mathrm{efl}}(\mathbf{r}, \mathbf{r}') \tag{32}$$

where $G^{\mathrm{ef\,sp}}$ is the effective saddle point contribution describing the ray fields in the effective medium, while the first and the second sums are the effective guided and leaky mode contributions denoted by superscripts "g" and "l," respectively.

The improper leaky modes are generated by poles on the lower Riemann sheet and are therefore not included in the proper (top Riemann sheet) spectrum pertaining to the field representations (29) and (31); however, as noted above, they can contribute (via the SDP deformation) to the asymptotic field.

Subject to the constraints formalized in Section IV-B, the effective asymptotic field solutions agree "acceptably well" with the actual asymptotic fields. The equivalence is demonstrated numerically in Section VI.

VI. Numerical Studies for Validation of the MRH Effective Fields

A. Test Configuration

New numerical results have been generated for the physical configuration in Fig. 1(b) comprising a vertical (z directed) electric dipole in the presence of a complex laminate slab occupying the region $0 \leq z \leq d$ in free space with an infinite (x, y) cross-section. All length scales are normalized to $d = 1$ (including the wavelength and the reference scale $\bar{d} = 1$). The frequency is specified indirectly by $k_0 d \xrightarrow{d=1} k_0 = 15$. Our test configuration involves an isotropic medium with a constant permeability μ and a multiscale permittivity $\varepsilon_z = \varepsilon_t \equiv \varepsilon$

$$\varepsilon = 2 + \sin(160\pi z^2) \quad \mu_z = \mu_t = 1, \quad 0 < z < 1. \tag{33}$$

The chirp-type heterogeneity in (33) comprises a continuum of scales from ~ 1 at $z = 0$ to 2^{-8} at $z = d = 1$ (see Fig. 3). Since $\varepsilon_{\max} = 3$ in (33), noting that $k_0 = 15$ and using (9) for K, we have $k_0 K \sim 26$ so that the homogenization parameter N_ν of (11) becomes small if the M-HS is chosen such that $\nu = M > 4$. The effective constitutive parameters calculated for two different values $\nu = 4$ and 6 of the M–HS $= 2^{-\nu}$ are shown in Fig. 4. One readily discerns the effective anisotropy implied by (8) and the finer resolution for $\nu = 6$. We note that the chirped narrow-scale smoothly continuous heterogeneity profile in (33) poses a greater challenge with respect to the actual-effective bounds than the wide-scale heterogeneity profile investigation in [28] and [29].

B. 1-D Green's Functions

As discussed in connection with (20), it is sufficient to consider only the fundamental spectral Green's functions $g^e_{Iv}(z, z'; \xi)$ and $g^h_{V\imath}(z, z'; \xi)$ for the E- and H-type modes, respectively. In fact the vertical electrical dipole excitation considered here is described entirely by g^e_{Iv}. However, in the framework of this section, we consider both g^e_{Iv} and $g^h_{V\imath}$ since they exhibit different multiresolution complexity, as discussed next.

The Green's function g^e_{Iv} satisfies (20), while $g^h_{V\imath}$ satisfies the dual equation with $(p^e, q^e) \leftrightarrow (q^h, p^h)$. For the constant μ case considered here, the equation for g^e_{Iv} has a more complicated structure than that for $g^h_{V\imath}$ since, referring to (5) and the $g^h_{V\imath}$ counterpart of (20), the heterogeneity in g^e_{Iv} appears only in the potential function, while in $g^e_{V\imath}$ it appears in both the derivative and the potential terms.

In Fig. 5, we compare the *actual* and the *effective* g^e_{Iv} solutions in (20) for a typical normalized spectral parameter $\xi = 0.5$. The numerical results show some error for $\nu = 4$ but excellent agreement for $\nu = 6$. Both solutions are generated via a direct numerical solution of (20) with either the actual or the effective heterogeneity functions.

Figs. 6 and 7 depict the dimensionless error estimator $\mathcal{E}_j$ in (12) of g^e_{Iv} and $g^h_{V\imath}$ as a function of the M-HS index ν. Actually, to verify the theoretical dependence of $\mathcal{E}_j$ on ν as predicted in (12), we present in Fig. 6 a normalized estimator obtained by multiplying $\mathcal{E}_j$ by $\bar{M}^2_{\nu=4}/\bar{M}^2_\nu$ where $\bar{M}_\nu$ and the reasons for this normalization are discussed in the next paragraph.

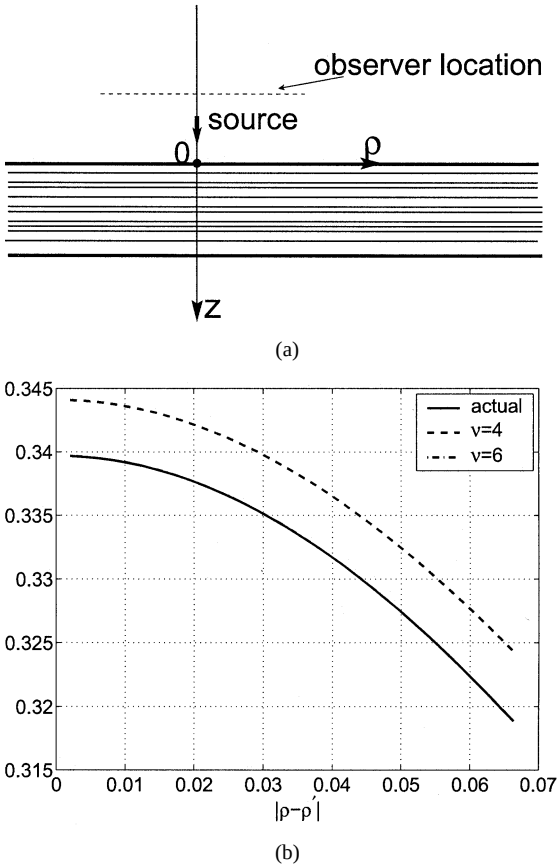

Fig. 12. 3-D reflected Green's function magnitude due to a dipole point source at $(x', y', z') = (0, 0, -0.1)$. (a) Physical configuration. (b) The field as a function of range ρ at the source level $z = -0.3$: The solid, dashed, and the dashed-dotted curves correspond to the actual solution and to the effective solutions for $\nu = 4$ and 6, respectively. The actual and $\nu = 6$ results coincide on the scale in these plots. Compare with the results for larger ρ in Fig. 13.

To explain the normalization in Fig. 6, we note that the bound in (12) includes the explicit dependence on ν via factor $2^{-\nu}$ as well as the factor M_ν that depends implicitly on ν. As defined in (13), M_ν is the ratio between the norm of the detail and smooth medium components. However, as follows from the derivation in [28, Sec. 5], M_ν is mainly affected by the norm of the detailed heterogeneities at the largest resolution level $2^{-(\nu+1)}$ (i.e., the largest scale neglected in the effective medium). Referring to (13), we tag this parameter by an overbar, i.e., $\bar{M}^2_\nu = \|q^d\|^2_\nu / \|q^{\mathrm{ef}}\|^2 + \|p^d\|^2_\nu / \|p^{\mathrm{ef}}\|^2$, where the subscript ν indicates the norm of the function at the resolution level $2^{-(\nu+1)}$. Clearly, $\bar{M}_\nu \leq M_\nu$ so that using $\bar{M}_\nu$ provides a tighter bound in (12), yet in (13) we preferred the more general form. Now we normalize $\mathcal{E}_j$ by $\bar{M}^2_\nu$ as indicated above, since the medium in (33) has a nonuniform distribution of the heterogeneities in the resolution levels (i.e., $\bar{M}_\nu$ varies with ν).

Indeed, one finds in Fig. 6 that $\mathcal{E}_j \bar{M}^2_{\nu=4}/\bar{M}^2_\nu$ exhibits a $2^{-2\nu}$ decay, as predicted by (12), provided that the M-HS is fine enough ($\nu \geq 4$) to justify the homogenization for $k_0 \approx 15$. Fig. 7 depicts $\mathcal{E}_j$ as a function of frequency, the M-HS$= 2^{-\nu}$ being kept constant with $\nu = 7$. One observes a $\sim k_0^3$ behavior as predicted by (12a) if one notes from (11) that N_ν increases like k_0 when ν is constant. Combining the results in Figs. 6 and

7, it follows that if ν is increased with increasing k_0 such that N_ν remains constant, then $\mathcal{E}_j$ is linear with k_0 as predicted in (12).

C. Spectral Equivalence

The equivalence of the discrete modal eigenvalues corresponding to the actual and the effective problems is explored in Fig. 9. At the given frequency, there are only five discrete eigenvalues representing five transversely propagating guided modes, but in this section we illustrate the quality of the analysis only for the $l = 1, 3$, and 5 modes. As discussed after (31), their accuracy plays a major role in tracking the 3-D modal field over large transverse distances (see also Fig. 11). Referring to (25b) and recalling the discussion concerning Fig. 6 above, the error $|\lambda_l - \lambda_l^{\rm ef}|$ as a function of ν, presented in Fig. 9(a), is normalized with respect to $\bar{M}_\nu^2$ (specifically, it is multiplied by $\bar{M}_{\nu=4}^2/\bar{M}_\nu^2$, where $\bar{M}_\nu$ is as defined in the previous section). The results in Fig. 9(a) for the $l = 1, 3$, and 5 eigenvalues show good agreement, which improves for the finer M-HS like $\sim 2^{-2\nu}$ as predicted in (25b).

Fig. 9(b) depicts the actual and effective eigenvalues (for $\nu = 4$ and 6) in the complex λ plane. Finally, the mode functions corresponding to the actual and effective formulations with $\nu = 4$ and $\nu = 6$ are depicted in Fig. 10. The eigenfunction accuracy is described by (25a), and its behavior is found to be similar to that of the source-excited fields in Fig. 7.

D. Total 3-D Fields

When the source and observation points are located inside or near the laminate and are laterally separated, the field is described most effectively by the z-domain spectral expansion (31) in Section V-B. The source location at $(x', y', z') = (0, 0, 0.5)$ inside the laminate is shown in Fig. 11(a); here, we have used the normalization $d = \bar{d} = 1$, and specify $k_0 d \to k_0 = 15$. Fig. 11(b)–(d) depicts cross-sectional cuts of the total 3-D Green's functions $|G|$ and $|G^{\rm ef}|$ at three transverse ranges: $k_0\rho = 0.5$, 2^9, and 2^{11}. The figures compare the effective solutions for $\nu = 4$ and 6 with the actual solutions.

In the near zone $(k_0\rho = 0.5)$, one needs to complement the guided mode series in the first term on the right-hand side of (31) with the continuous spectrum integral in the second term, which was generated by direct evaluation (point-wise summation) of the integral. Note the fine details of the field near the source in Fig. 11(b), which cannot be achieved by summation over the discrete modes of Fig. 10 alone (there are five guided modes for the values of k_0 and d in the present example; only three of them are depicted in Figs. 9 and 10). The continuous spectrum models the near-zone ρ-evanescent spectra that are not accounted for in the propagation modes of Fig. 10. The final results depicted in Fig. 11(b) show excellent agreement (better than the figure resolution) between the actual and effective GFs for the finer M-HS $(\nu = 6)$. In the intermediate and far zones (for large $|z - z'|$), the contribution of the continuous spectrum (i.e., the effect of the "leaky" and the "evanescent" modes) is weak and may be neglected; the field is now mainly described by the discrete propagating modes. There are two sources of

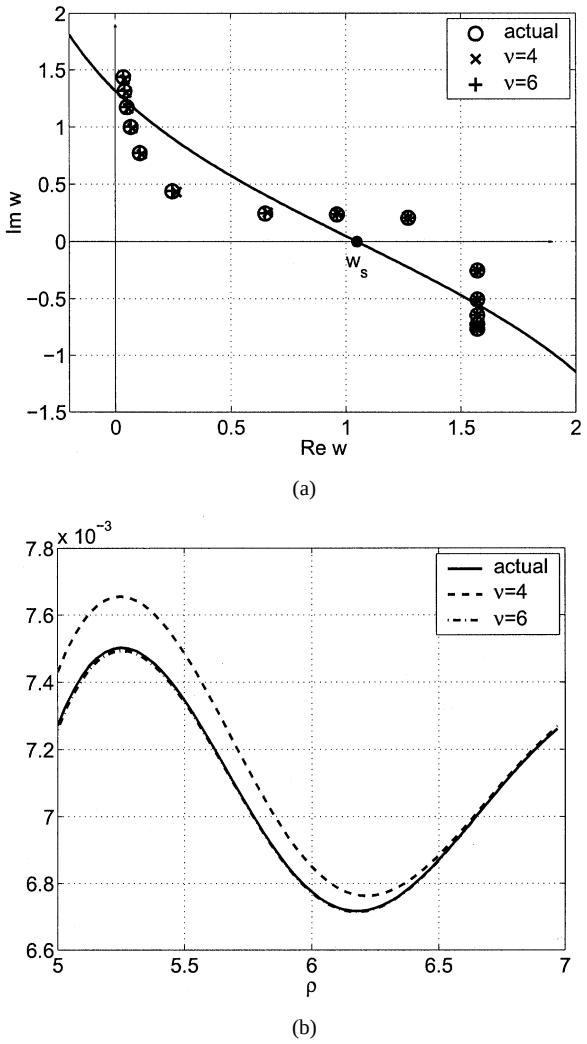

Fig. 13. Asymptotic field evaluation for large lateral displacement ρ, corresponding to the configuration in Fig. 12. (a) Complex w-plane plot (defined by $\sin w = \xi$) shows the guided wave poles (along the $\mathrm{Re}\, w = \pi/2$ axis), the leaky wave poles (in the first quadrant of the w-plane), the saddle point w_s, and the corresponding SDP. The singularities of the effective problem with $\nu = 6$ are indistinguishable from the actual poles within the scale of the figure and are identified by "$\circ$." The singularities of effective problem with $\nu = 4$ are identified by "$\times$." (b) 3-D reflected field calculated via (32), using the spectral constituents of (a). Solid curve: actual solution; dashed-dotted curve: effective solution for $\nu = 6$ (indistinguishable on the scale of the figure); dashed curve: effective solution for $\nu = 4$.

error: one is associated with the eigenfunction error in Fig. 10; it affects the field structure but does not accumulate with range. The other source is the accumulation of the modal phase error $k_0|\xi_l - \xi_l^{\rm ef}|\rho \sim k_0|\lambda_l - \lambda_l^{\rm ef}|(2\xi_l)^{-1}\rho$, which becomes dominant in the intermediate and far zones. From Fig. 9(a), the eigenvalue error is largest for $l = 1$ where, from Fig. 9(b), $\xi_{l=1} \approx 1.3$. For $\nu = 4$, we have from Fig. 9(a) that $|\lambda_1 - \lambda_1^{\rm ef}| \sim 2^{-10}$, while for $\nu = 6$, we use the normalization $\bar{M}_{\nu=4}^2/\bar{M}_{\nu=6}^2 = 0.1065$ to estimate $|\lambda_1 - \lambda_1^{\rm ef}| \sim 2^{-14}/0.1065$. The distance where the phase error becomes ≈ 0.5 is therefore estimated to be $k_0\rho \approx 2^{10}$ and $\approx 2^{11}$ for the coarse and fine M-HS, $\nu = 4$ and 6, respectively. Indeed, the results in Fig. 11(c) for $k_0\rho = 2^9$ show excellent agreement between the actual and effective solutions when $\nu = 6$ and a certain error for $\nu = 4$, which is mainly due to the eigenfunction error noted above. The long-range results in

Fig. 11(d) for $k_0\rho = 2^{11}$ show acceptable distortion for $\nu = 6$ but very substantial distortion for $\nu = 4$ due to the intermode phase error accumulation.

When the source and observation points lie outside the laminate as in Fig. 12(a), the field is best described by the z-propagation expansion in (28) and (29). For a point dipole at $z' = -0.1$, $\boldsymbol{\rho}' = \mathbf{0}$, and observations on the plane $z = -0.3$, Fig. 12(b) displays the reflected field as a function of the transverse displacement ρ, for two values of the M-HS: $\nu = 4$ and $\nu = 6$. The finer homogenization evidently yields better agreement.

The results in Fig. 12(b), which were calculated by straightforward numerical integration (Riemann summation) of (29), become numerically sensitive for large lateral displacement ρ where it is advantageous to parameterize the field asymptotically via (32). The outcomes are plotted in Fig. 13 for the same configuration as in Fig. 12 but for larger ρ. Fig. 13(a) exhibits the SDP and the spectral singularities of the actual and effective problems. They are shown in the complex-angle plane w, defined by $\sin w = \xi = \sqrt{-\lambda}$. Identified are the guided wave poles (along the $\mathrm{Re}w = \pi/2$ axis), the leaky wave poles (in the first quadrant of the w-plane that corresponds to the lower Riemann sheet in the λ plane), the saddle point w_s (which defines the geometrically reflected ray), and the corresponding SDP. The pole singularities of the effective problem with the finer M-HS ($\nu = 6$) are indistinguishable on the scale of the figure from the actual pole locations and are denoted by "$\circ$." The effective poles for $\nu = 4$ are denoted by $\times$.

For large $k_0\rho$, the conventional Sommerfeld integration contour is deformed into the SDP through the saddle point w_s in Fig. 13(a). The field is then given by the SDP contribution plus the contributions from the poles that are intercepted during the contour deformation. These are the leaky wave and the guided wave poles on the left-hand side of the SDP [see Fig. 13(a)].

The value of $|G|$ for two values of ν calculated from (32) in terms of the spectral constituents (saddle point and relevant guided and leaky poles) of Fig. 13(a) is depicted in Fig. 13(b) as a function of the lateral displacement for $\rho > 4$ [see Fig. 12(a), which depicts the field for $\rho < 2$]. As expected, the effective solution (dashed-dotted curve) for the finer M-HS with $\nu = 6$ performs better than that for the coarser M-HS with $\nu = 4$ (dashed curve) and is, in fact, indistinguishable from the actual field (solid curve).

VII. Concluding Remarks

In this first part of a two-part paper, we are concerned with the multiresolution homogenization of field-network representations, we have endeavored to extract from the formal mathematical treatment of MRH in [28] and [29] those "pragmatic" effective measures that allow conventional field representations in the presence of multilayered dielectric slabs to be converted directly to corresponding representations for MRH-smoothed fields. A detailed summary of this process was provided in Section I. Since the accuracy of the actual-effective equivalence of these formulations depends critically on error assessments, we have performed a representative set of new numerical experiments that involve sensitivity studies with respect to parametric variations pertaining to a particular, but highly instructive, model micro-macro-scale laminate. Whereas, conclusions in the earlier investigations [28], [29] are based on relatively sparse preliminary numerics, the validations here provide a substantially better understanding of the performance capabilities of our approach. The foundation has thereby been laid for the judicious applications of MRH field theory to the construction of an effective network theory for interconnected multiscale conglomerates, which will be carried out in Part II [34].

Appendix A

A Summary of Multiresolution Analysis (MRA)

Let $\{\mathbb{V}_j\}_{j\in\mathbb{Z}}$ be a nested sequence of linear spaces dense in $\mathbb{L}_2$, and let $\phi(z)$, $\psi(z)$ be the corresponding scaling and wavelet functions, respectively. The functions $\phi_{jn}(z)$ and $\psi_{mn}(z)$ are defined via

$$\phi_{jn}(z) = \left(\frac{2^j}{\bar{d}}\right)^{\frac{1}{2}} \phi\left(\frac{2^j z}{\bar{d}} - n\right)$$
$$\psi_{mn}(z) = \left(\frac{2^m}{\bar{d}}\right)^{\frac{1}{2}} \psi\left(\frac{2^m z}{\bar{d}} - n\right). \tag{A1}$$

The set of functions $\{\phi_{jn}\}_{n\in\mathbb{Z}}$ is an orthonormal basis of $\mathbb{V}_j$, and the set of functions $\{\psi_{jn}\}_{n\in\mathbb{Z}}$ is an orthonormal basis of $\mathbb{W}_j$, which is the orthogonal complement of $\mathbb{V}_j$ in $\mathbb{V}_{j+1}$.

The MRA is called r-regular if for $\forall N \geq 1$ and $0 \leq l \leq r$, $\phi(z)$ and $\psi(z)$ satisfy

$$\left|\partial_z^l \phi(z)\right|, \left|\partial_z^l \psi(z)\right| \leq C_N \left(1 + \left|\frac{z}{\bar{d}}\right|\right)^{-N}. \tag{A2}$$

This condition describes both the regularity of the MRA and its localization. The regularity is also related to the "cancellation property." If $\phi(z)$ and $\psi(z)$ constitute r-regular MRA, then the wavelet has $r+1$ vanishing moments

$$\int z^n \psi(z) dz = 0; \quad n = 0, 1, \ldots, r. \tag{A3}$$

A function $f(z) \in \mathbb{L}_2$ can then be written as the sum of its smooth and detail coefficients

$$f(z) = f^s(z) + f^d(z) \tag{A4}$$

where

$$f^s(z) = \mathcal{P}_j f = \sum_n s_{jn}\phi_{jn}(z)$$
$$s_{jn} = \langle f, \phi_{jn}\rangle \tag{A5a}$$
$$f^d(z) = \mathcal{D}_j f = \sum_{mn} d_{mn}\psi_{mn}(z)$$
$$d_{mn} = \langle f, \psi_{mn}\rangle \tag{A5b}$$

where $\mathbf{s} = \{s_{jn}\}_{n\in\mathbb{Z}}$ and $\boldsymbol{d} = \{d_{mn}\}_{mn\in\mathbb{Z}}$ with $m = j, \ldots, \infty$ define the MRA expansion coefficients.

Further discussions on the localization, regularity properties, and characterization of functional spaces can be found in [19] and [20].

REFERENCES

[1] L. B. Felsen, "Hybrid ray-mode fields in inhomogeneous waveguides and ducts," *J. Acoust. Soc. Amer.*, vol. 69, no. 2, pp. 352–361, 1981.

[2] L. B. Felsen and A. Kamel, "Hybrid ray-mode formulation of parallel plane waveguide Green's functions," *IEEE Trans Antennas Propagat.*, vol. AP-29, pp. 637–649, 1981.

[3] A. Kamel and L. B. Felsen, "On the ray equivalent of a group of modes," *J. Acoust. Soc. Amer.*, vol. 71, pp. 1445–1452, 1982.

[4] ——, "Hybrid Green's function for SH motion in a low velocity layer," *Wave Motion*, vol. 5, pp. 83–97, 1983.

[5] L. B. Felsen, "Progressing and oscillatory waves for hybrid synthesis of source-excited propagation and diffraction," *Trans. Antennas Propagat.*, vol. AP-32, pp. 775–796, 1984.

[6] L. B. Felsen and N. Marcuvitz, *Radiation and Scattering of Waves*. Piscataway, NJ: IEEE Press, 1994.

[7] L. M. Brekhovskikh, *Waves in Layered Media*. New York: Academic, 1980.

[8] W. C. Chew, *Waves and Fields in Inhomogeneous Media*. Piscataway, NJ: IEEE Press, 1995.

[9] L. B. Felsen, "Novel ways for tracking rays," *J. Opt. Soc. Amer. A*, vol. 2, pp. 954–965, 1986.

[10] J. M. Arnold and L. B. Felsen, "Spectral reconstruction of uniformized wavefields from nonuniform ray or adiabatic mode forms for acoustic propagation and diffraction," *J. Acoust. Soc. Amer.*, vol. 87, pp. 587–600, 1990.

[11] B. Z. Steinberg, E. Heyman, and L. B. Felsen, "Phase space beam summation for time-harmonic radiation from large apertures," *J. Opt. Soc. Amer. A*, vol. 8, pp. 41–59, 1991.

[12] ——, "Phase space beam summation for time dependent radiation from large apertures: continuous parametrization," *J. Opt. Soc. Amer. A*, vol. 8, pp. 943–958, 1991.

[13] E. Heyman and L. B. Felsen, "Gaussian beam and pulsed beam dynamics: complex source and spectrum formulations within and beyond paraxial asymptotics," *J. Opt. Soc. Amer. A*, vol. 18, pp. 1588–1611, 2001.

[14] A. Bensoussan, J. L. Lions, and G. Papanicolaou, *Asymptotic Analysis for Periodic Structures*. Amsterdam, the Netherlands: North-Holland, 1978.

[15] V. V. Jikov, S. M. Kozlov, and O. A. Oleinik, *Homogenization of Differential Operators and Integral Functionals*. Berlin, Germany: Springer-Verlag, 1994.

[16] M. E. Brewster and G. Beylkin, "A multiresolution strategy for numerical homogenization," *Appl. Comp. Har. Anal.*, vol. 2, pp. 327–349, 1995.

[17] A. C. Gilbert, "A comparison of multiresolution and classical one-dimensional homogenization schemes," *Appl. Comp. Har. Anal.*, vol. 5, pp. 1–35, 1998.

[18] G. Beylkin and N. Coult, "A multiresolution strategy for reduction of elliptic PDE's and eigenvalue problems," *Appl. Comp. Har. Anal.*, vol. 5, pp. 129–155, 1998.

[19] I. Daubechies, "Ten lectures on wavelets," in *CBMS-NSF Series in Applied Mathematics*. Philadelphia, PA: SIAM, 1992.

[20] Y. Meyer, *Wavelets and Operators*. Cambridge, U.K.: Cambridge Univ. Press, 1992.

[21] B. Z. Steinberg and J. J. McCoy, "Toward local effective parameter theories using multiresolution decomposition," *J. Acoust. Soc. Amer.*, vol. 96, pp. 1130–1143, 1994.

[22] ——, "Effective measures for nonstationary microscale stiffness variation using multiresolution decomposition," *J. Acoust. Soc. Amer.*, vol. 98, no. 6, pp. 3516–3526, 1995.

[23] ——, "A class of one dimensional stiffness microstructures resulting in identical macroscale response," *Wave Motion*, vol. 23, pp. 237–258, 1996.

[24] ——, "A multiresolution study of effective properties of complex electromagnetic systems," *IEEE Trans. Antennas Propagat.*, vol. 26, pp. 971–981, 1998.

[25] B. Z. Steinberg, J. J. McCoy, and M. Mirotznik, "A multiresolution approach to homogenization and effective modal analysis of complex boundary value problems," *SIAM J. Appl. Math.*, vol. 60, no. 3, pp. 939–966, 2000.

[26] B. Z. Steinberg, "Homogenization and effective properties formulations for propagation in finely structured laminates—a multi-resolution approach," *Wave Motion*, vol. 34, no. 3, pp. 319–337, 2001.

[27] V. Lomakin and B. Z. Steinberg, "Effective resonance representation of propagators in complex ducts—A multiresolution homogenization approach," *IEEE Trans. Antennas. Propagat.*, vol. 51, pp. 2754–2760, Sept. 2003.

[28] V. Lomakin, B. Z. Steinberg, and E. Heyman, "Multiresolution homogenization for radiation and propagation in multiscale laminates: Part I—Effective formulation," , submitted for publication.

[29] ——, "Multiresolution homogenization for radiation and propagation in multiscale laminates: Part II—Spectral representations of the field," , submitted for publication.

[30] ——, "UWB analysis of EM fields in complex laminates: an MRA homogenization approach," in *Ultra-Wideband, Short-Pulse Electromagnetics 5*, P. D. Smith, Ed. New York: Plenum, 2001.

[31] ——, "Analysis of the multi-resolution time domain (MRTD) method via the multi-resolution homogenization (MRH) theory," in *Proc. URSI Trianum Int. Symp. Electromagnetic Theory*, Victoria, Canada, May 2001, pp. 396–398.

[32] B. Z. Steinberg and E. Heyman, "Effective vertical modes and horizontal rays for wave propagation in complex inhomogeneous ducts," in *Proc. URSI Trianum Int. Symp. Electromagnetic Theory*, Thessloniki, Greece, 1998.

[33] V. Lomakin, B. Z. Steinberg, and E. Heyman, "A multi-resolution homogenization (MRH) analysis for the fields near the interface between complex laminates," in *XXVIIth General Assembly Int. Union Radio Science (URSI)*, Maastricht, the Netherlands, Aug. 2002.

[34] V. Lomakin, B. Z. Steinberg, E. Heyman, and L. B. Felsen, "Multi-resolution homogenization of field and network formulations for multi-scale laminate dielectric slabs—Part II: Network theory," *IEEE Trans. Antennas. Propagat.*, to be published.

[35] R. F. Harrington, *Field Computation by Moment Methods*. New York: IEEE Press, 1993.

[36] L. B. Felsen, M. Mongiardo, and P. Russer, "Electromagnetic field representations and computations in complex structures I: Complexity architecture and generalized network formulation," *Int. J. Numer. Model.*, vol. 15, pp. 93–107, 2002.

[37] ——, "Electromagnetic field representations and computations in complex structures II: Alternative Green's functions," *Int. J. Numer. Model.*, vol. 15, pp. 109–125, 2002.

[38] P. Russer, M. Mongiardo, and L. B. Felsen, "Electromagnetic field representations and computations in complex structures III: Network representations of the connection and subdomain circuits," *Int. J. Numer. Model.*, vol. 15, pp. 127–145, 2002.

[39] L. D. Faddeyev, "The inverse problem in the quantum theory of scattering," *J. Math. Phys.*, vol. 4, pp. 72–104, 1963.

Vitaliy Lomakin was born in January 26, 1975. He received the M.Sc. degree in electrical engineering from Kharkov State University, Ukraine, in 1996 and the Ph.D. degree in electrical engineering from Tel Aviv University, Israel, in 2003.

From 1997 to 2002, he was a Teaching Assistant in the Department of Electrical Engineering, Tel Aviv University. From 2000 to 2002, he was also with Xellant Inc., Israel, working on antennas for mobile communication. Currently, he is a Postdoctoral Associate at the Center for Computational Electromagnetics, University of Illinois at Urbana-Champaign. His research interests are in analytic methods in wave theory, effective properties of complex (multiscale) objects, antenna analysis and design, and computational electromagnetics.

Ben Z. Steinberg (M'94–SM'99) was born in Tel-Aviv, Israel, in October 1957. He received the B.Sc., M.Sc., and Ph.D. degrees in electrical engineering from the Faculty of Engineering, Tel-Aviv University, Israel, in 1983, 1985, and 1989, respectively.

From 1989 to 1991, he held a Postdoctoral position at the School of Engineering, The Catholic University of America, Washington, DC. Since October 1991, he has been with the Department of Interdisciplinary Studies Faculty of Engineering, Tel-Aviv University, where he is currently an Associate Professor. His research interests include analytical methods, modeling, and numerical algorithms in wave theory. This includes high-frequency techniques, beam methods, and phase-space representations for time harmonic and transient wave phenomena.

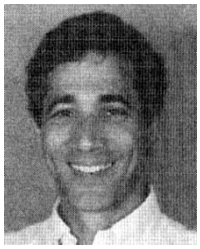

Ehud Heyman (S'80–M'82–SM'88–F'01) was born in Tel Aviv, Israel, in 1952. He received the B.Sc. degree in electrical engineering from Tel Aviv University, Israel (*summa cum laude*) as Valedictorian, the M.Sc. degree in electrical engineering (with distinction) from the Technion—Israel Institute of Technology, Haifa, and the Ph.D. degree in electrophysics from the Polytechnic Institute of New York (now Polytechnic University), Brooklyn, in 1977, 1979, and 1982, respectively.

In 1983, he joined the Department of Physical Electronics of the Faculty of Engineering, Tel Aviv University where he is now a Professor of electromagnetic theory and Heads the Department of Physical Electronics. From 1991 to 1992, he was on sabbatical at Northeastern University, Boston, MA, the Massachusetts Institute of Technology, Cambridge, and the A. J. Devaney Association, Boston. He spent several summers as a Visiting Professor at Chuo University, Tokyo, Japan, the Eindhoven University of Technology, Northeastern University, and the Polytechnic Institute. He has published over 70 articles and has been an Invited Speaker at many international conferences. His research interests involve analytic methods in wave theory, including high-frequency and time-domain techniques for propagation and scattering, short-pulse antennas, pulsed beams and directed energy transfer, inverse scattering and target identification, imaging and synthetic aperture radar propagation in random medium.

Prof. Heyman is a Member of Sigma Xi and the Chairman of the Israeli National Committee for Radio Sciences (URSI). He is an Associate Editor of the IEEE Press Series on Electromagnetic Waves and was an Associate Editor of the IEEE/APS MAGAZINE. While at the Polytechnic Institute he was a Research Fellow and later a Postdoctoral Fellow, as well as a Rothschild, a Fullbright, and a Hebrew Technical Institute Fellow.

Leopold B. Felsen (S'47–M'54–SM'55–F'62–LF'90) was born in Munich, Germany, on May 7, 1924. He received the B.E.E., M.E.E, and D.E.E. degrees from the Polytechnic Institute of Brooklyn, Brooklyn, NY, in 1948, 1950, and 1952, respectively. He emigrated to the United States in 1939 and served in the U.S. Army from 1943 to 1946. After 1952, he remained with the Polytechnic (now Polytechnic University), gaining the position of University Professor in 1978. From 1974 to 1978, he was Dean of Engineering. In 1994, he resigned from the full-time Polytechnic faculty and was granted the status of University Professor Emeritus. He is now Professor of Aerospace and Mechanical Engineering and Professor of Electrical and Computer Engineering at Boston University, Boston, MA (part-time). He is the author or coauthor of over 350 papers and of severa1 books, including the classic *Radiation and Scattering of Waves* (Piscataway, NJ: IEEE Press, 1994). He is an Associate Editor of severa1 professional journals and an Editor of the *Wave Phenomena Series* (New York: Springer-Verlag). His research interests encompass wave propagation and diffraction in complex environments and in various disciplines, high-frequency asymptotic and short-pulse techniques, and phase-space methods with an emphasis on wave-oriented data processing and imaging.

Dr. Felsen received the the Guggenheim Fellowship in 1973, the Humboldt Foundation Senior Scientist Award in 1981, the IEEE/APS best paper award for 1969, and was coauthor for 1974, 1981, the R. W. P. King Award for 1984, 1986, and 2000, the Balthasar van der Pol Gold Medal from the International Union of Radio Science (URSI) in 1975, an honorary doctorate from the Technical University of Denmark in 1979, an IEEE Centennial Medal in 1984, the IEEE Heinrich Hertz Gold Medal for 1991, the APS Distinguished Achievement Award for 1998, the IEEE Third Millenium Medal in 2000 (nomination by APS), the IEEE Electromagnetics Award for 2003, and three Distinguished Faculty Alumnus Awards from Polytechnic University. In 1974 he was an IEEE/APS (Antennas and Propagation Society) Distinguished Lecturer. In 1977, he was elected to the National Academy of Engineering. He is a Member of Sigma Xi and a Fellow of the Optical Society of America and the Acoustical Society of America. He has held named Visiting Professorships and Fellowships at universities in the United States and abroad. His Poet's Corner appears sporadically in the IEEE/APS MAGAZINE. He has served on the APS Administrative Committee from 1963–1966, and was Vice Chairman and Chairman for both the United States (1966–1973) and the International (1978–1984) URSI Commission B.